Biophysical Journal
Article

Biophysical Society

GRPY: An Accurate Bead Method for Calculation of Hydrodynamic Properties of Rigid Biomacromolecules

Pawel J. Zuk,[1,2] Bogdan Cichocki,[3] and Piotr Szymczak[3,*]
[1]Department of Biosystems and Soft Matter, Institute of Fundamental Technological Research, Polish Academy of Sciences, Warsaw, Poland; [2]Department of Mechanical and Aerospace Engineering, Princeton University, Princeton, New Jersey; and [3]Institute of Theoretical Physics, Faculty of Physics, University of Warsaw, Warsaw, Poland

ABSTRACT Two main problems that arise in the context of hydrodynamic bead modeling are an inaccurate treatment of bead overlaps and the necessity of using volume corrections when calculating intrinsic viscosity. We present a formalism based on the generalized Rotne-Prager-Yamakawa approximation that successfully addresses both of these issues. The generalized Rotne-Prager-Yamakawa method is shown to be highly effective for the calculation of transport properties of rigid biomolecules represented as assemblies of spherical beads of different sizes, both overlapping and nonoverlapping. We test the method on simple molecular shapes as well as real protein structures and compare its performance with other computational approaches.

INTRODUCTION

Precise calculation of hydrodynamic properties of macromolecules is crucial for the correct interpretation of the results of experimental studies of solution structure and dynamics of biopolymers, such as fluorescence correlation spectroscopy, ultracentrifugation, or dynamic light scattering. There is extensive literature discussing various techniques used in hydrodynamic modeling (1–8). Early approaches to this problem were based on the approximation of the macromolecule by a simple shape such as a sphere or ellipsoid (9–12), the hydrodynamic properties of which can be calculated analytically. However, many biomolecules have irregular shapes that cannot be represented by simple geometric forms, which necessitates the use of more sophisticated numerical methods.

Several approaches to this problem have emerged over the years. The most popular of these are bead modeling (13–15), direct calculation using boundary element method (16,17), and path integral techniques (18–20). For the recent detailed reviews and discussions of hydrodynamic modeling, the reader is referred to the work of Rocco and Byron (21) as well as the book (8), with separate chapters on HYDRO (22), BEST (23), and UltraScan Solution Modeler (US-SOMO) (24) program suites as well as an introductory chapter by Byron (25).

Briefly, in boundary element methods, one represents the flow field in terms of boundary distributions of fundamental solutions of a given differential equation. The densities of the distributions are then computed to satisfy the respective boundary conditions on the surface of the macromolecule. In the context of Stokes equations, the boundary element method has been utilized since 1978, when Youngren and Acrivos used it to study the problem of a Stokes flow in the presence of a solid particle (26). In recent years, it has become increasingly popular (27) because the vast increase of computing power has allowed for the calculation of hydrodynamic properties of even relatively large macromolecules. In this respect, the BEST method by Aragon (7,17) has emerged as a dominant performer.

On the other hand, the ZENO algorithm uses path integral techniques to calculate some of the scalar hydrodynamic properties of complex particles (18–20), by exploiting analogies between hydrodynamics and electrostatics. The macromolecule is enclosed within a sphere, from the surface of which a large number of random walks are launched toward the surface of the molecule. Based on the fraction of the walks that reaches the surface, the values of friction coefficient and intrinsic viscosity can be estimated to within 2–5% accuracy. The main advantage of this method is its large speed and relatively low computational complexity.

Submitted December 4, 2017, and accepted for publication July 16, 2018.
*Correspondence: piotr.szymczak@fuw.edu.pl
Editor: James Cole.
https://doi.org/10.1016/j.bpj.2018.07.015

Finally, in bead modeling (13–15), which is the focus of our study, the shape of a macromolecule is approximated by a number of small spheres either filling the volume of a molecule or covering its surface. The hydrodynamic properties of such a conglomerate are then calculated by a method originating from Kirkewood and Riseman: by applying forces to individual beads and then calculating the flow field around them based on the known solutions for the flow around the sphere. This approach has been successfully used over the years to calculate the hydrodynamic characteristics of macromolecules, particularly thanks to the effort of de la Torre and colleagues, who have created the HYDRO suite of programs (28,29). Bead modeling, although elegant and successful in a broad range of applications, is not without its problems. The most significant of these is that the Kirkwood-Riseman formalism fails whenever some of the beads are significantly larger than the others (30) and in particular gives a vanishing viscosity for a single sphere. This necessitated the introduction of a number of semiempirical, shape-dependent correction factors (29). Another deficiency of the existing bead models is that they run into problems whenever the beads overlap, particularly if they are different in size (31,32). In such cases, a phenomenological Zipper-Durchschlag formula for the translational diffusivity is usually used (33), which, however, lacks continuity and does not have the proper limiting behavior, as one bead becomes fully immersed inside the other (34). Alternatively, the overlaps are removed, e.g., by resizing the spheres (32), which, however, affects the accuracy of bead covering.

Recently, we have devised a self-consistent scheme of deriving hydrodynamic matrices that addresses all of the above issues (34–36). The scheme generalizes the well-established Rotne-Prager-Yamakawa approximation, which incorporates all the long-ranged, nonintegrable terms in the expansion in the inverse distance between the beads, corresponding to $(a/r)^{\alpha}$, $\alpha \leq 3$, where a is the bead radius. In contrast to previous approaches, our method relies on the direct integration of force densities over the sphere surfaces. This turns out to provide the correct limiting behavior of the mobilities for the touching spheres and for a complete overlap with one sphere immersed in the other one. Additionally, the inclusion of dipolar components of the hydrodynamic interaction tensors allows for a direct calculation of the intrinsic viscosity without the need of introducing correcting factors. As a result, we obtain an effective and versatile tool, capable of handling a large variety of different bead models both for nonoverlapping and overlapping beads. The latter are particularly attractive, as they allow for a faithful representation of a macromolecular shape using a significantly smaller number of beads than the nonoverlapping models.

The work is organized as follows. First, we briefly review the theoretical foundations of the generalized Rotne-Prager-Yamakawa (GRPY) method. Next, we show how to calculate hydrodynamic properties within this formalism. Then, the method is applied to simple geometric shapes as well as a number of real protein structures. Finally, we give a short description of the numerical implementation of the method. An open-source FORTRAN code calculating hydrodynamic properties of biomolecules is distributed as Supporting Material to the manuscript. The code can take as an input a bead covering produced by other algorithms, but it also provides its own covering of overlapping beads based on the PDB file of the protein.

METHODS

Hydrodynamic interactions

We represent the macromolecule as a collection of N rigidly connected beads of different radii a_i, which can potentially overlap. Due to the small size of the biomolecules, the fluid flow around them is in the low Reynolds number regime and can be described by the stationary Stokes equations

$$\eta_s \nabla^2 \boldsymbol{v} - \nabla p = 0 \tag{1}$$

and

$$\nabla \cdot \boldsymbol{v} = 0, \tag{2}$$

where η_s is the viscosity of the solvent. The linearity of the Stokes equations implies a linear relation between the force and velocity moments

$$\begin{pmatrix} \tilde{\boldsymbol{F}} \\ \tilde{\boldsymbol{T}} \\ \tilde{\boldsymbol{S}} \end{pmatrix} = -\begin{pmatrix} \boldsymbol{\zeta}^{tt} & \boldsymbol{\zeta}^{tr} & \boldsymbol{\zeta}^{td} \\ \boldsymbol{\zeta}^{rt} & \boldsymbol{\zeta}^{rr} & \boldsymbol{\zeta}^{rd} \\ \boldsymbol{\zeta}^{dt} & \boldsymbol{\zeta}^{dr} & \boldsymbol{\zeta}^{dd} \end{pmatrix} \cdot \begin{pmatrix} \tilde{\boldsymbol{v}}_\infty - \tilde{\boldsymbol{U}} \\ \tilde{\boldsymbol{\omega}}_\infty - \tilde{\boldsymbol{\Omega}} \\ \tilde{\boldsymbol{E}}_\infty \end{pmatrix}. \tag{3}$$

Here, $\tilde{\boldsymbol{F}} = (\boldsymbol{F}_1, \boldsymbol{F}_2, \ldots, \boldsymbol{F}_N)$ is the $3N$ dimensional vectors of forces that the beads exert on the fluid and analogously for the torques $\tilde{\boldsymbol{T}}$. The translational and rotational velocities of the particles ($\tilde{\boldsymbol{U}}$ and $\tilde{\boldsymbol{\Omega}}$) are written in the same manner. Next, $\tilde{\boldsymbol{v}}_\infty = (\boldsymbol{v}_\infty(\boldsymbol{R}_1), \ldots, \boldsymbol{v}_\infty(\boldsymbol{R}_N))$ are the values of external flow velocity calculated at the centers of the particles, $\boldsymbol{R}_i$. Similarly, $\tilde{\boldsymbol{\omega}}_\infty$ gives the vector of vorticities at the centers of the particles, with $\boldsymbol{\omega}_\infty = (1/2)\nabla \times \boldsymbol{v}_\infty$. Finally, $\tilde{\boldsymbol{E}}_\infty = (\mathbf{E}_\infty(\boldsymbol{R}_1), \ldots, \mathbf{E}_\infty(\boldsymbol{R}_N))$ is the vector of strain rates, with $\boldsymbol{E}_\infty = 1/2(\nabla \boldsymbol{v}_\infty + (\nabla \boldsymbol{v}_\infty)^T)$. The vector $\boldsymbol{E}_\infty$ is $5N$-dimensional because of the symmetric character of strain tensors. The last element, $\tilde{\boldsymbol{S}} = (\mathbf{S}_1, \ldots, \mathbf{S}_N)$ is the vector of particle stresses, again $5N$-dimensional. The superscripts t, r, and d in Eq. 3 denote translational, rotational, and dipolar components of the grand friction matrix $\boldsymbol{\zeta}$. A partial inversion of Eq. 3 defines the grand mobility matrix $\boldsymbol{\mu}$,

$$\begin{pmatrix} \tilde{\boldsymbol{U}} - \tilde{\boldsymbol{v}}_\infty \\ \tilde{\boldsymbol{\Omega}} - \tilde{\boldsymbol{\omega}}_\infty \\ -\tilde{\mathbf{S}} \end{pmatrix} = \begin{pmatrix} \boldsymbol{\mu}^{tt} & \boldsymbol{\mu}^{tr} & \boldsymbol{\mu}^{td} \\ \boldsymbol{\mu}^{rt} & \boldsymbol{\mu}^{rr} & \boldsymbol{\mu}^{td} \\ \boldsymbol{\mu}^{dt} & \boldsymbol{\mu}^{dr} & \boldsymbol{\mu}^{dd} \end{pmatrix} \cdot \begin{pmatrix} \tilde{\boldsymbol{F}} \\ \tilde{\boldsymbol{T}} \\ \tilde{\boldsymbol{E}}_\infty \end{pmatrix}, \tag{4}$$

again, with the translational, rotational, and dipolar components.

So far, we have not used the fact that the macromolecule—represented as a conglomerate of beads—moves as a rigid body. The friction matrix of such an object will be 11×11 tensor defined by a relation analogous to Eq. 3. This time, however, it involves $\boldsymbol{U}_c$, $\boldsymbol{\Omega}_c$, and $\boldsymbol{E}_c$—the translational and rotational velocities of a conglomerate as well as the strain rate at its center. The assumption of the rigid body motion allows us to link these parameters with the velocities of the individual beads, e.g.,

$$\boldsymbol{U}_i = \boldsymbol{U}_c + \boldsymbol{\Omega}_c \times (\boldsymbol{R}_i - \boldsymbol{R}_0), \tag{5}$$

where $\boldsymbol{R}_0$ is the reference point with respect to which the translation and rotation are defined. As discussed in detail in the Appendix, this allows us to find the relation between $\boldsymbol{\zeta}_c$ and the N-body grand friction matrix $\boldsymbol{\zeta}_N$ of the form

$$\boldsymbol{\zeta}_c = \boldsymbol{T}_N(\boldsymbol{R}_0)^T \cdot \boldsymbol{\zeta}_N \cdot \boldsymbol{T}_N(\boldsymbol{R}_0), \tag{6}$$

where $\boldsymbol{T}_N$ is the operator linking bead velocities with those of the macromolecule. This operator is given by Eq. A3.

The construction of hydrodynamic matrices proceeds now as follows. First, we find the N-body friction matrix $\boldsymbol{\zeta}_N$. Subsequently, the friction matrix of a macromolecule is obtained by projection given by Eq. 6. Finally, $\boldsymbol{\zeta}_c$ is partially inverted to yield the rigid-body grand mobility matrix $\boldsymbol{\mu}_c$. The translational and rotational components of the mobility matrix of conglomerate are linked with the respective diffusion matrices via Einstein-Smoluchowski relations. This defines the translational diffusion matrix

$$\boldsymbol{D}^t = k_B T \boldsymbol{\mu}_c^{tt} \tag{7}$$

as well as its rotational counterpart

$$\boldsymbol{D}^r = k_B T \boldsymbol{\mu}_c^{rr}. \tag{8}$$

The projection operator $\boldsymbol{T}_N(\boldsymbol{R}_0)$ in Eq. 6 involves an arbitrary reference point $\boldsymbol{R}_0$. A natural question that can be raised in this context is whether the choice of $\boldsymbol{R}_0$ has an effect on the elements of the rigid body matrices $\boldsymbol{\zeta}_c$ and $\boldsymbol{\mu}_c$. As it turns out, the answer is different for different components of these matrices. Translational and rotational components of the grand mobility matrix have been analyzed in Kim and Karrila (37) and it has been shown that $\boldsymbol{\mu}_c^{tt}$, $\boldsymbol{\mu}_c^{tr}$, and $\boldsymbol{\mu}_c^{rt}$ depend on the choice of the origin, whereas $\boldsymbol{\mu}_c^{rr}$ does not. Generalizing this reasoning to dipolar components leads to the conclusion that $\boldsymbol{\mu}_c^{dd}$, $\boldsymbol{\mu}_c^{dr}$, and $\boldsymbol{\mu}_c^{rd}$ are not origin sensitive (36).

Generalized Rotne-Prager-Yamakawa approximation

In this section, we summarize the GRPY approach for the calculation of hydrodynamic matrices. The key role in this approximation is played by another hydrodynamic tensor—a full inverse of the grand friction matrix, $\boldsymbol{m} = \boldsymbol{\zeta}^{-1}$, introduced by (38). This tensor links force and velocity multipoles:

$$\begin{pmatrix} \tilde{\boldsymbol{v}}_\infty - \tilde{\boldsymbol{U}} \\ \tilde{\boldsymbol{\omega}}_\infty - \tilde{\boldsymbol{\Omega}} \\ \tilde{\boldsymbol{E}}_\infty \end{pmatrix} = -\begin{pmatrix} \boldsymbol{m}^{tt} & \boldsymbol{m}^{tr} & \boldsymbol{m}^{td} \\ \boldsymbol{m}^{rt} & \boldsymbol{m}^{rr} & \boldsymbol{m}^{td} \\ \boldsymbol{m}^{dt} & \boldsymbol{m}^{dr} & \boldsymbol{m}^{dd} \end{pmatrix} \cdot \begin{pmatrix} \tilde{\boldsymbol{F}} \\ \tilde{\boldsymbol{T}} \\ \tilde{\mathbf{S}} \end{pmatrix}. \tag{9}$$

The next step is to analyze the relation between the velocities of particles moving in a Stokes flow and induced force density localized on particle surfaces:

$$[\boldsymbol{U}_i + \boldsymbol{\Omega}_i \times \boldsymbol{\rho}_i - \boldsymbol{v}_\infty(\boldsymbol{r})]_{\boldsymbol{r}\in S_i} = \sum_j \int \boldsymbol{T}_0(\boldsymbol{r}-\boldsymbol{r}') \cdot \boldsymbol{f}_j(\boldsymbol{r}')\mathrm{d}^3\boldsymbol{r}'. \tag{10}$$

Here, $\boldsymbol{\rho}_i = \boldsymbol{r} - \boldsymbol{R}_i$, with $\boldsymbol{R}_i$ denoting the position of particle i. Next, $-\boldsymbol{f}_j(\boldsymbol{r}')$ is the density of the forces exerted by the particle j on the fluid. Finally, $\boldsymbol{T}_0$ is the Oseen tensor

$$\boldsymbol{T}_0(\boldsymbol{r}) = \frac{1}{8\pi\eta_s r}(\mathbf{1} + \hat{\boldsymbol{r}}\hat{\boldsymbol{r}}), \tag{11}$$

which is the Green function for the Stokes problem for unbounded space. The key idea behind the GRPY approximation is to describe the force density in terms of its three multipoles only:

$$\boldsymbol{f}_j = \boldsymbol{w}_j^t \cdot \boldsymbol{F}_j + \boldsymbol{w}_j^r \cdot \boldsymbol{T}_j + \boldsymbol{w}_j^d : \boldsymbol{S}_j, \tag{12}$$

where $\boldsymbol{w}_j^p$ are operators associated with different multipoles ($p = t,r,d$)

$$\boldsymbol{w}_j^t(\boldsymbol{r}) = \frac{1}{4\pi a_j^2}\mathbf{1}\delta(\rho_j - a_j), \quad \boldsymbol{w}_j^r(\boldsymbol{r}) = \frac{3}{8\pi a_j^3}\boldsymbol{\varepsilon} \cdot \hat{\boldsymbol{\rho}}_j \delta(\rho_j - a_j),$$
$$\boldsymbol{w}_j^d(\boldsymbol{r}) = \frac{3}{4\pi a_j^3}\delta(\rho_j - a_j)\hat{\boldsymbol{\rho}}_j \cdot \boldsymbol{\mathcal{I}}. \tag{13}$$

In the above, $[\boldsymbol{\varepsilon}\cdot\hat{\boldsymbol{\rho}}]_{\alpha\beta} = \varepsilon_{\alpha\beta\gamma}[\hat{\boldsymbol{\rho}}_j]_\gamma$ and $\boldsymbol{\mathcal{I}}$ is the fourth-rank isotropic tensor, traceless and symmetric in its first and last index pairs:

$$\mathcal{I}_{\alpha\beta\delta\gamma} = \frac{1}{2}\left(\delta_{\alpha\delta}\delta_{\beta\gamma} + \delta_{\alpha\gamma}\delta_{\beta\delta} - \frac{2}{3}\delta_{\alpha\beta}\delta_{\delta\gamma}\right). \tag{14}$$

Next, the velocity field in the left hand side of Eq. 10 is approximated by a linear flow. The multipoles characterizing this flow (velocity, $\boldsymbol{U}_i - \boldsymbol{v}_\infty(\boldsymbol{R}_i)$; vorticity, $\boldsymbol{\Omega}_i - \boldsymbol{\omega}_\infty$; and strain rate, $-\boldsymbol{E}_\infty(\boldsymbol{R}_i)$) can be obtained from $[\boldsymbol{U}_i + \boldsymbol{\Omega}_i \times \boldsymbol{\rho}_i - \boldsymbol{v}_\infty(\boldsymbol{r})]_{\boldsymbol{r}\in S_i}$ by integration of this expression multiplied by the transposed $\boldsymbol{w}_i^p$ operators. This leads to the following relation for the elements of the inverse friction matrix:

$$\boldsymbol{m}_{ij}^{pq} = \langle \boldsymbol{w}_i^p \,|\, \boldsymbol{T}_0 \,|\, \boldsymbol{w}_j^q \rangle = \iint [\boldsymbol{w}_i^p(\boldsymbol{r}')]^T \cdot \boldsymbol{T}_0(\boldsymbol{r}'-\boldsymbol{r}'') \cdot \boldsymbol{w}_j^q(\boldsymbol{r}'')\mathrm{d}^3\boldsymbol{r}'\mathrm{d}^3\boldsymbol{r}'', \tag{15}$$

where we have used Eq. 9 together with Eq. 12. In the above, T stands for the transpose. The explicit formulas for the elements of the inverse friction matrix, calculated based on Eq. 15, can be found in (36). Importantly, the integrals in Eq. 15 can be calculated both for overlapping and nonoverlapping beads, which—as shown in (34–36)—leads to the self-consistent description of hydrodynamic properties of the system over the entire range of interparticle distances. In particular, this approximation exhibits a correct limiting behavior at a complete overlap, with one sphere fully immersed in the other—the mobility of such a system reduces to that of an external sphere.

The GRPY approximation of the inverse friction matrix outlined above can be seen as a generalization and extension of the Stokesian dynamics method developed by Durlofsky, Brady, and Bossis (38,39). Their focus was, however, on the suspension of freely moving, nonoverlapping particles, whereas this formalism is aimed at the calculation of hydrodynamic matrices for rigidly connected beads, both overlapping and nonoverlapping. On the other hand, a similar construction of the hydrodynamic matrices for rigid macromolecules has been carried out by Goldstein (40), with two important differences: 1) he considered rotational and translational degrees of freedom only, and 2) in the case of overlapping spheres, he derived the hydrodynamic matrices for the case of equal sphere radii only.

RESULTS AND DISCUSSION

Translational and rotational diffusion

Translational diffusion provides information on the relaxation of particle positions caused by the Brownian motion. To assess it, we mark the point on the molecule, $\boldsymbol{R}_0$, and

follow its mean-square displacement in the laboratory frame, $\langle(\boldsymbol{R}(t)-\boldsymbol{R}(0))^2\rangle$, where $\langle\ldots\rangle$ denotes the equilibrium average and $\boldsymbol{R}(0)=\boldsymbol{R}_0$. Importantly, due to the coupling between the rotational and translational motion, the mean-square displacement is in general not linear in time except at very short and long times. This linearity allows us to define the short-time and long-time translational diffusion coefficient using the relations

$$\left\langle(\boldsymbol{R}(t)-\boldsymbol{R}(0))^2\right\rangle \sim 6D_s^t(\boldsymbol{R}_0)t, \quad t\to 0 \tag{16}$$

and

$$\left\langle(\boldsymbol{R}(t)-\boldsymbol{R}(0))^2\right\rangle \sim 6D_l^t t, \quad t\to\infty, \tag{17}$$

respectively. For intermediate times, the mean-square displacement is no longer linear in time, involving a combination of three exponential modes, e^{-t/τ_i}, with

$$\tau_1^{-1}=D_2^r+D_3^r,\ \ \tau_2^{-1}=D_1^r+D_3^r,\ \ \tau_3^{-1}=D_1^r+D_2^r, \tag{18}$$

where D_1^r, D_2^r, and D_3^r are the eigenvalues of $\boldsymbol{D}^r$, corresponding to rotational diffusion coefficients around the main axes of rotation (41). The explicit expression for the mean-square displacement valid over the entire time range is given in Appendix B. The presence of rotational timescales in MSD confirms that the nonlinearities in this dependence are indeed due to rotational-translational couplings. Using Eq. 18, we can formalize the criterion for the short- and long-time diffusion regimes as $t \ll \min t_i$ and $t \gg \max t_i$, respectively. For a typical biomacromolecule, the rotational relaxation timescales, τ, are on the order of a microsecond. Thus, most of the measurements of the diffusion in biomolecules (e.g., through dynamic light scattering or fluorescence correlation spectroscopy) captures the long-time diffusion coefficient D_l^t.

The short-time translational diffusion coefficient is linked to the trace of the translational diffusion tensor calculated at $\boldsymbol{R}_0$,

$$D_s^t(\boldsymbol{R}_0)=\frac{1}{3}\mathrm{Tr}\boldsymbol{D}^t(\boldsymbol{R}_0), \tag{19}$$

which makes it dependent on the choice of the reference point. In the above, $\boldsymbol{D}^t(\boldsymbol{R}_0)$ stands for the translational diffusion matrix of a conglomerate, Eq. 7, obtained from the N-body mobility matrix by the projection operation (Eq. A2) with $\boldsymbol{R}_0$ as the reference point.

The long-time diffusion coefficient, on the other hand, is independent of the choice of a reference point and is given by

$$D_l^t = D_{mc}\equiv\frac{1}{3}\mathrm{Tr}\boldsymbol{D}^t(\boldsymbol{R}_{mc}), \tag{20}$$

where $\boldsymbol{R}_{mc}$ is the so-called mobility center—a point at which the translational-rotational mobility matrix, $\boldsymbol{\mu}^{tr}$, is symmetric. The unique property of the mobility center is that the mean square displacement of this point is linear over the entire time range:

$$\left\langle(\boldsymbol{R}_{mc}(t)-\boldsymbol{R}_{mc}(0))^2\right\rangle = 6D_{mc}t. \tag{21}$$

Another way of assessing D_l^t is through centrifugation or sedimentation of the macromolecules. The sedimentation coefficient $s=v_t/g$ is a ratio of particle terminal sedimentation velocity to its acceleration due to centrifugation or gravity:

$$s=\frac{MD_l^t}{N_A k_B T}(1-\rho\bar{v}), \tag{22}$$

where M is the molecular mass, N_A is Avogadro number, $\bar{v}$ is the specific volume of the macromolecule, and ρ the density of the solvent.

Intrinsic viscosity

Another important tool for probing macromolecular conformations is the viscosity measurement. Suspended particles increase the viscous dissipation in the bulk flow due to the stresses acting on their surfaces. Intrinsic viscosity, $[\eta]$, is defined by means of the following relationship for the viscosity of a dilute suspension:

$$\eta=\eta_s(1+[\eta]c+\ldots). \tag{23}$$

In the above, viscosity is decomposed into the contribution from the solvent alone, η_s, and the contribution from the particles proportional to their mass concentration, c. In theoretical hydrodynamics, intrinsic viscosity is sometimes defined by the expansion in the volume fraction (i.e., fraction of volume occupied by the particles) instead of mass concentration. This leads to dimensionless intrinsic viscosity, which can be obtained by

$$[\tilde{\eta}]=[\eta]/\bar{v}. \tag{24}$$

In the above, $\bar{v}$ is the specific volume of the macromolecule given by $\bar{v}=N_A V/M$, where V is the volume of the molecule.

Viscosity is in general frequency-dependent, as epitomized by the experiments with a Couette viscometer under oscillatory flow conditions in which one observes that η increases as the frequency of the oscillations decrease. This effect is a manifestation of a Brownian contribution to the viscosity related to the relaxation of particle orientations due to Brownian motion. Accordingly, viscosity can be cast as a sum of the high frequency term $[\eta]_\infty$ and the Brownian $[\eta]_\omega^B$ contribution (42,43):

$$[\eta]_\omega=[\eta]_\infty+[\eta]_\omega^B. \tag{25}$$

The Brownian contribution can be written as the sum of five modes,

$$[\eta]^B_\omega = \frac{N_A k_B T}{10 M \eta_s} \sum_{j=1}^{5} \frac{A_j}{i\omega + f_j}, \tag{26}$$

which are given explicitly in Appendix B. Note that this contribution has a nonzero imaginary part, which reflects a phase shift between the stress and strain rate. The frequencies f_j are again related to the relaxation times of the Brownian rotational motion (see Eq. C1). The high-frequency regime can then be associated with $\omega \gg \max f_j$, whereas the low-frequency regime corresponds to $\omega \ll \min f_j$.

At large frequencies, the Brownian contribution vanishes, and intrinsic viscosity approaches its high-frequency asymptote

$$[\eta]_\infty = \frac{N_A}{10 M \eta_s} \sum_{\alpha\beta} \left(\mu_c^{dd}\right)_{\alpha\beta\beta\alpha}, \tag{27}$$

which is directly linked to the dipolar component of the mobility matrix averaged over all orientations of the macromolecule. On the other hand, the zero-frequency limit can be obtained by adding $[\eta]^B_{\omega=0}$ to the above term.

$$[\eta]_0 = \frac{N_A}{10 M \eta_s} \left(\sum_{\alpha\beta} \left(\mu_c^{dd}\right)_{\alpha\beta\beta\alpha} + k_B T \sum_{j=1}^{5} \frac{A_j}{f_j} \right). \tag{28}$$

It is the latter, zero-frequency viscosity that is relevant experimentally, because the experimental time scales are typically much longer than the relaxation times of the Brownian rotational motion.

As already mentioned, the dipolar components of the mobility matrix do not depend on the choice of the reference point. However, in some of the alternative approaches to the calculation of intrinsic viscosity, one finds that the result is origin sensitive (1,14), and it is proposed that $\boldsymbol{R}_0$ needs to be chosen in such a way as to guarantee the minimal energy dissipation (the so-called "viscosity center," $\boldsymbol{R}_\eta$). A possible reason for this discrepancy is that the macromolecular viscosity in these studies is expressed not in terms of $\boldsymbol{\mu}_c^{dd}$, as in Eq. 27, but rather through the friction tensor $\boldsymbol{\zeta}_c^{dd}$:

$$[\eta]^\zeta(\boldsymbol{R}_0) = \frac{N_A}{10 M \eta_s} \sum_{\alpha\beta} \left(\zeta_c^{dd}\right)_{\alpha\beta\beta\alpha}(\boldsymbol{R}_0), \tag{29}$$

the elements of which depend on the choice of origin. Strikingly, if the friction tensor in Eq. 29 is calculated in the viscosity center, one finds that $[\eta]^\zeta(\boldsymbol{R}_\eta) \approx [\eta]_0$. The two sides become indistinguishable in case of the molecules of high symmetry, for which the translational-dipolar coupling becomes negligible. A relevant example here is that of a dumbbell, which consists of two rigidly connected beads. If their sizes are equal, then both the mobility and viscosity center coincide with the geometric center of the dumbbell. In this case, $\boldsymbol{\zeta}^{td} = 0$ and $[\eta]^\zeta(\boldsymbol{R}_\eta) = [\eta]_0$.

However, if the beads are of different sizes, the viscosity center is shifted with respect to the mobility center ($\boldsymbol{\zeta}^{td} \neq 0$), and the values of $[\eta]^\zeta(\boldsymbol{R}_\eta)$ and $[\eta]_0$ no longer coincide. In Fig. 1, we show the relative difference between $[\eta]_0$ and $[\eta]^\zeta$ for a dumbbell comprised of two beads of different radii, a_1 and a_2. Two different cases are considered: a dumbbell with the beads touching ($l = a_1 + a_2$), and the one in which $l = 2a_1$. As observed, the difference between $[\eta]_0$ and $[\eta]^\zeta$ remains relatively small, on the order of 0.1%. The difference disappears either when the dumbbell becomes a single sphere ($a_2 \to 0$) or when the two beads are of an equal size.

Next, we analyze the dependence of intrinsic viscosity on the distance between the beads. This time, we take a symmetric rigid dumbbell with two beads of radius a separated by a distance l. The data presented in Fig. 2 shows both high- and low-frequency viscosity calculated using the GRPY approach together with the results of HYDRO++ calculations.

These results are compared with the results of the virtually exact multipole expansion method (44–47), which generalizes Eqs. 9 and 10 to include a larger number of force and velocity multipoles, N_{mult}. The multipole method employs the multiple scattering expansion, which involves summing up the infinite number of reflections of the Stokes flow between all of the particles. The flows calculated in this way include the higher-order singular and regular solutions of the Stokes equation that are generated during successive reflections. In this framework, the RPY approximation corresponds to a single scattering only and thus involves pairs of particles and never larger groups. In practice, the multipole method converges quickly to the analytical solution of Stokes equations. For example, for a rigid dumbbell

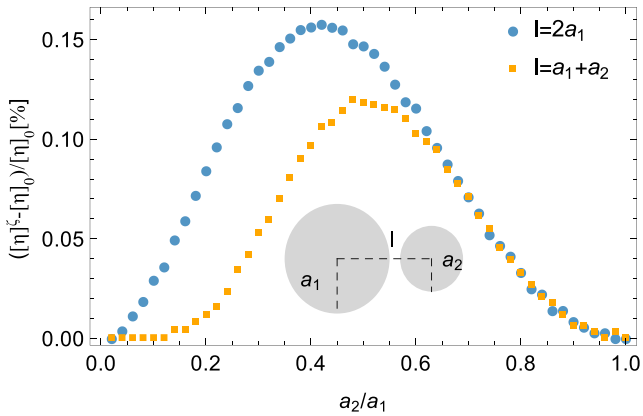

FIGURE 1 Relative difference between the viscosity calculated using Eqs. 28 and 29 for an asymmetric dumbbell with beads of size a_1 and $a_2 < a_1$ and the distance between their centers l. Orange points correspond to the dumbbell with the touching beads, whereas blue points correspond to the situation in which $l = 2a_1$. To see this figure in color, go online.

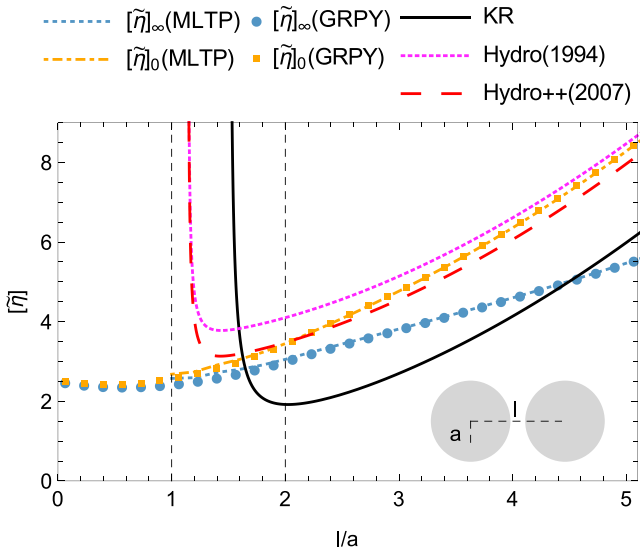

FIGURE 2 Dimensionless intrinsic viscosity, $[\tilde{\eta}]$, of the rigid dumbbell as a function of the bead separation normalized by the radius, l/a. The vertical lines denote points at which the beads touch ($l = 2a$) and when the center of one bead becomes immersed in the second one ($l = a$). The data points show high- and low-frequency viscosity calculated using the GRPY approach (*orange* and *blue points*, respectively) as well as the results of the Kirkwood-Riseman-based approaches: original Kirkwood-Riseman method (Eq. 31; (14,49)), HYDRO package with volume correction to viscosity (28), and HYDRO++ code (29). Additionally, we show the results calculated using the multipole method. To see this figure in color, go online.

consisting of equal, touching spheres, intrinsic viscosity can be calculated analytically (11,48) to yield $[\tilde{\eta}]_\infty = 3.4496$, whereas at $l = 7.5244a$, the viscosity increases to $[\tilde{\eta}]_\infty = 14.756$. The corresponding results calculated using multipole expansion with 360 multipole components (which corresponds to L = 10 in the notation of Cichocki et al. (46)) per particle give 3.4494 at touching and 14.756 for $l = 7.5244a$; hence, the relative accuracy is better than 10^{-4}. However, because of its computational complexity, the multipole method is not suitable for calculating the hydrodynamic properties of real biomolecules.

Referring to Fig. 2, we note the differences between the traditional bead methods (represented by HYDRO) and GRPY. The reason is that HYDRO uses a simplified approach to calculate viscosity, which does not involve the dipolar components of either a friction or mobility matrix. Instead, an idea originating from Kirkwood and Riseman is used, with viscosity calculated as (49):

$$[\eta] = -\frac{N_A}{M\dot{\gamma}\eta_s}\sum_i \langle (\boldsymbol{F}_i \cdot \mathbf{e}_x)(\boldsymbol{R}_i \cdot \mathbf{e}_y)\rangle \qquad (30)$$

where the shear flow of the form $\boldsymbol{v}_\infty = \dot{\gamma} y \mathbf{e}_x$ is assumed, and the angular brackets denote the average over all possible orientations of the macromolecule with respect to the flow. Next, $\boldsymbol{F}_i$ are the forces exerted by the fluid on the beads related to their velocities by the formula analogous to Eq. 4,

$$\tilde{\boldsymbol{U}} - \tilde{\boldsymbol{v}}_\infty = \boldsymbol{\mu}^{tt} \cdot \tilde{\boldsymbol{F}}, \qquad (31)$$

but without taking into account either rotational or dipolar terms. The velocities of the beads are then calculated based on Eq. A2, and relation 31 is inverted to yield F_i with the reference point chosen at the viscosity center. Unfortunately, the lack of dipolar terms in Eq. 31 results in somewhat erratic behavior when the number of beads is small or if some of the beads are significantly larger than the others (30). In particular, it gives a vanishing intrinsic viscosity for a single bead instead of $[\eta] = 5/2\overline{v}$, as derived by Einstein. This deficiency can be partially fixed by the introduction of an ad hoc volume correction in which a term equal to $\frac{5}{2}\frac{V}{M}N_A$ is added to the viscosity, with V standing for the total volume of the beads. Later on, it was noticed that such an approach significantly overestimates viscosity and an extra multiplying factor needed to be introduced (29).

Earlier versions of HYDRO code run into similar problems while calculating rotational diffusivity of the macromolecules, because—as pointed put by Goldstein (40)—they did not include rotational degrees of freedom in the mobility matrix. However, this was later corrected in (29), and the rotational degrees of freedom have been introduced in the 3RD procedure of HYDRO++, which eliminated the need for volume correction for rotation.

Coming back to the results of Fig. 2, we observe that the original Kirkwood-Riseman method (Eq. 30) underestimates the intrinsic viscosity of the dumbbell; however, it correctly captures the asymptotic slope of the $[\tilde{\eta}](l/a)$ dependence.

The volume corrections introduced in the 1994 version of the HYDRO package bring the values of the viscosity closer to the correct asymptote, but as the separation between the beads decreases, the agreement gets progressively worse. Further multiplicative factors introduced in HYDRO++ improve the agreement at intermediate distances at the cost of somewhat worse performance at a larger l. Strikingly, both HYDRO and HYDRO++ fail to capture the $\eta(l)$ dependence for overlapping beads. The Kirkwood-Riseman approaches in this regime lead to divergent results, whereas GRPY exhibits correct limiting behaviors at a complete overlap of the spheres, as discussed in (36).

An additional advantage of the GRPY scheme is that it allows for the separation of the Brownian and non-Brownian contributions to low-frequency intrinsic viscosity as given by Eq. 28, which is not possible in the Kirkwood-Riseman approach. In general, the more the shape of the molecule deviates from a spherical one, the more important the Brownian contribution becomes. For example, for a rod comprised of 10 touching beads, the Brownian contribution is responsible for 50% of the total.

Kirkwood-Riseman approaches improve their performance for systems comprising a larger number of beads,

as then the number of force centers in Eq. 31 increases, which better approximates the overall force distribution. This is confirmed by the analysis of rod-like molecules built from N touching spheres (Fig. 3). Similar to the previous case, the original KR method produces a correct slope but underpredicts the magnitude of $[\tilde{\eta}]$ by ~5/2. This correction, although constant in magnitude, constitutes a decreasing fraction of the total viscosity with increasing N. This discrepancy is to a large extent fixed by the introduction of additive volume correction in the HYDRO package and an additional multiplicative factor in HYDRO++. However, for small numbers of beads, there are still marked differences between the viscosities reported by these models and the exact values.

Hydrodynamic properties of simple shaped molecules

To demonstrate the effectiveness of the GRPY approach, we have calculated the diffusion coefficients for a number of basic shapes, comprising touching beads of equal radii a (the notation follows (29)):

LN: N beads positioned along a straight line,
RN: N beads placed in the vertices of regular N-polygons,
PN: N beads placed in the vertices of regular N-polyhedrons.

Table 1 presents the translational and rotational diffusion coefficients as well as the dimensionless intrinsic viscosities for shapes calculated using the GRPY method, the most recent version (10) of the HYDRO++ package by de la Torre et al. (29), and the ZENO algorithm implemented within the US-SOMO package (24). Additionally, we compare these results to the multipole expansion method, which we treat as a benchmark. The values of D_t and D_r are normalized by the translational and rotational diffusivities of a single bead, i.e., $D_0^t = k_B T/6\pi\eta a$ and $D_0^r = k_B T/8\pi\eta a^3$, respectively. Out of a number of different methods of calculating diffusion coefficients offered by HYDRO++ package, we have chosen the 3RD method, which uses the Rotne-Prager approximation for translational and rotational degrees of freedom (the other methods offered within HYDRO++ yielded significantly less accurate results).

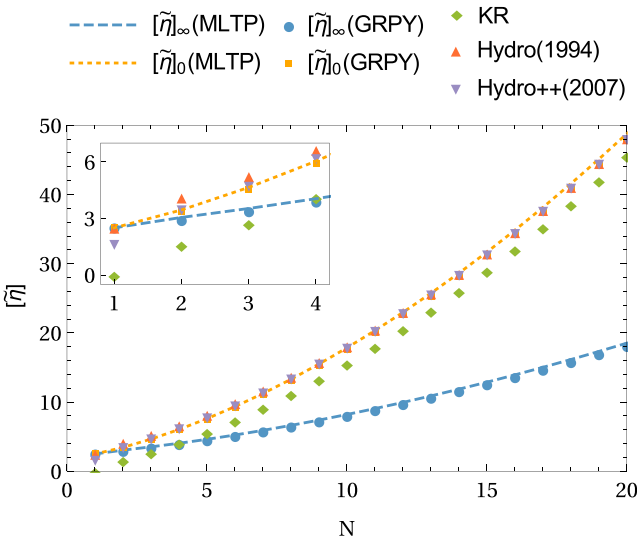

FIGURE 3 Dimensionless intrinsic viscosity, $[\tilde{\eta}]$, of the rigid rod of touching spheres as a function of the sphere count N. To see this figure in color, go online.

Let us first consider diffusion coefficients. As it is seen, even though the general performance of all of the approaches (ZENO, HYDRO++, and GRPY) is quite satisfactory, the values calculated using ZENO and GRPY are the closest to the benchmark results, followed by HYDRO++. An improved performance of GRPY with respect to the standard Rotne-Prager-Yamakawa approximation used in HYDRO++ is related to the fact that within GRPY, the approximation is performed on the inverse friction matrix $\boldsymbol{m}$. In the standard Rotne-Prager-Yamakawa approximation, on the other hand, the formula analogous to Eq. 15 is used to represent the mobility matrix, $\boldsymbol{\mu}$. Importantly, if one starts with the $\boldsymbol{m}$ matrix calculated using the GRPY approach and uses it to compute the mobility matrix, one recovers all of the terms in the expansion in the inverse distance between the beads corresponding to the standard Rotne-Prager-Yamakawa approximation as well as a number of additional terms related to higher multipoles. The presence of the latter is the reason why, in general, GRPY performs better than the standard Rotne-Prager-Yamakawa approach.

Next, we turn to intrinsic viscosity. The data in Table 1 shows that in this case, the GRPY method performs better than either ZENO or the HYDRO++ package. The results of GRPY systematically underestimate the intrinsic viscosity by no more than 3%, whereas those of HYDRO++ can be both larger and smaller than the exact values, with the scatter up to 8%. Errors of similar magnitude are observed in the results of ZENO. In Table 1, we also compare the low-frequency viscosity calculated based on the mobility and friction-based formulae, Eqs. 28 and 29, respectively. As evidenced by the data in the table, for the molecules that are symmetric about their centers (i.e., all the shapes except for the triangle and tetrahedron), both ways of estimating the viscosity give equivalent results. For the triangle (R3) and tetrahedron (P4), the equivalence no longer holds, but the differences remain small, on the order of 1%.

Complex biorelevant shapes

Because the focus of this contribution is on the hydrodynamic properties of real biomolecules, we now turn to protein structures. An important issue that one encounters when calculating the hydrodynamic properties of macromolecules is the hydration effect (50–52). Namely, as pointed out by

TABLE 1 Hydrodynamic Properties of Simple Geometric Shapes

	ZENO		HYDRO++			GRPY					MLTP			
Shape	D^t/D_0^t	$[\tilde{\eta}]_0$	D^t/D_0^t	D^r/D_0^r	$[\tilde{\eta}]_0$	D^t/D_0^t	D^r/D_0^r	$[\tilde{\eta}]_\infty$	$[\tilde{\eta}]_0$	$[\tilde{\eta}]^\zeta$	D^t/D_0^t	D^r/D_0^r	$[\tilde{\eta}]_\infty$	$[\tilde{\eta}]_0$
L2	0.722 (7)	3.3 (2)	0.735	0.367	3.35	0.723	0.367	3.0	3.42	3.42	0.718	0.363	3.05	3.45
L5	0.433 (4)	7.6 (4)	0.441	0.103	7.38	0.437	0.103	4.56	7.54	7.54	0.430	0.102	4.62	7.60
L10	0.279 (2)	18.3 (9)	0.283	0.046	17.4	0.282	0.046	8.08	17.6	17.6	0.277	0.045	8.20	17.8
R3	0.622 (7)	3.4 (2)	0.634	0.224	3.66	0.619	0.221	3.26	3.475	3.481	0.616	0.216	3.34	3.55
R4	0.547 (5)	3.7 (2)	0.560	0.152	3.90	0.546	0.149	3.49	3.823	3.823	0.542	0.146	3.59	3.91
R6	0.442 (5)	4.7 (2)	0.455	0.078	4.66	0.444	0.076	4.21	4.819	4.819	0.439	0.075	4.33	4.93
R8	0.375 (5)	5.9 (2)	0.383	0.045	5.7	0.376	0.044	5.10	6.058	6.058	0.371	0.043	5.24	6.21
P4	0.565 (5)	3.3 (2)	0.575	0.178	3.65	0.562	0.169	3.38	3.384	3.395	0.560	0.166	3.47	3.47
P6	0.496 (5)	3.3 (2)	0.502	0.125	3.55	0.492	0.116	3.38	3.38	3.38	0.490	0.114	3.48	3.48
P8	0.433 (5)	3.7 (2)	0.438	0.083	3.82	0.429	0.0769	3.83	3.816	3.816	0.427	0.0753	3.94	3.94
P12	0.389 (5)	3.3 (2)	0.396	0.063	3.48	0.387	0.058	3.49	3.495	3.495	0.385	0.056	3.60	3.60
P20	0.245 (2)	7.3 (4)	0.254	0.016	7.51	0.250	0.015	7.80	7.798	7.798	0.250	0.015	7.89	7.89

Hydrodynamic properties of N-spheres in line (LN), regular N-polygons (RN) and N-polyhedrons (PN): normalized diffusion coefficients and dimensionless intrinsic viscosity calculated using ZENO (19) (with 10^9 random walk trajectories) implemented within US-SOMO package (24), HYDRO++ package (29), the GRPY method and the multipole (MLTP) method with 105N multipole components. For ZENO calculations, the last digit gives the uncertainty, e.g. $0.722(7) = 0.722 \pm 0.007$.

various researchers, the nature of the layer of water at the surface of a macromolecule is different from the bulk water, with an increased viscous dissipation. Hydration effectively increases the surface at which the no-slip boundary condition has to be satisfied, shifting it by ~1 Å toward the bulk.

There are several implementations of a hydration layer in the computational literature. Some approaches (such as HydroPro (53) or BEST (17)) are using a hydration layer of a uniform thickness. Another approach is to rescale the radii of the beads by a constant scale factor (AtoB (31)) or use a nonuniform, amino-acid-dependent thickness of hydration layer (e.g., SOMO (4,6)), calculated based on the average number of water molecules hydrating an amino acid (54) multiplied by the effective volume of water molecule of 24 $Å^3$ (55). A similar approach to the construction of hydrated bead covering is taken in this study. Taking as an input the PDB file with the protein structure, we use the *MSMS* package (56) to identify the atoms on the surface of the protein, discarding all the rest. This speeds up the calculations while at the same time not decreasing the accuracy because inner atoms are screened from the flow by the external ones. Next, also using *MSMS*, we assign van der Waals radii to all the atoms and group them according to the residue to which they belong. Note that some of the residues can have just a single surface atom, whereas others might not be present at the surface at all. For each residue, the additional volume resulting from hydration, V_h, is then calculated as the mean number of hydrating water molecules (54) times the effective water molecule volume. Next, we distribute this water volume in equal proportion among atoms that are at the surface by increasing their radii. Note that due to the fact that the beads corresponding to different atoms in a given residue overlap, the total hydration volume of the residue obtained by this procedure is smaller than V_h. To correct for this, we rescale the hydration shells of the atoms such that the overall hydration volume of a residue approaches V_h.

Such a procedure (which we call hydrated-atom bead covering, or "h-atom") is partly inspired by an earlier model by Venable and Pastor (57), who have represented a protein as a collection of beads placed at the coordinates of heavy atoms and screened the accessible surface area to identify the exposed atoms contributing to friction. We also draw inspiration from Rai et al. (4) in that we utilize the hydration numbers by Kuntz Jr. and Kauzmann (54) in assigning the water molecules to each accessible residue.

In general, h-atom produces bead covering with overlaps between the beads. However, GRPY can handle overlaps without problems, and thus there is no need for the overlap reduction procedures sometimes used in other approaches. In SOMO, for example, the overlapping beads are removed by fusing them, moving them away from each other, or resizing (4,6) while care is taken to preserve the topography of the outer surface. The resizing can either be performed hierarchically (two beads with the largest overlap are resized first and then the others) or synchronously (all of the overlapping beads are scaled by a certain factor, then the ensemble is rescreened, and resizing is repeated) (6,24). The GRPY method can also work with bead coverings produced by other algorithms, both overlapping and nonoverlapping. In Tables 2 and 3, we provide a detailed comparison of diffusivities and intrinsic viscosities calculated by different methods and models based on the structures analyzed in previous works. We also quote the results of experimental measurements of these quantities as well as provide the mean-square deviation of the theoretical predictions of different methods with respect to the experimental values. Additionally, we calculate the mean error of the theoretical prediction, which allows us to assess whether a given method systematically over- or underestimates the experimental value. If, for

TABLE 2 Comparison of Translational Diffusion Coefficients of Different Proteins Calculated Using Various Bead Coverings and Computational Methods with the Experimental Measurements

					Relative Error ΔD^t (%)				
					AtoB G2			AtoB G5	
Protein	PDB	Mass [kDa]	$D^{t,\exp}[10^{-7}$ cm^2/s]	References	SMI	ZENO	GRPY	SMI	ZENO
Cytochrome C	1HRC	12.34	12	(5,68–72)	−0.17	−0.17	−2	−1	−1.8
Ribonuclease A	8RAT	13.68	12	(6)	0.86	0.86	−0.6	0	0
α-Lactalbumin bovine	1HFX	14.26	11	(5,73,74)	7.7	7.7	5.8	6.8	6.8
Lysozyme	1E8L(n)	14.31	11	(4,6,75–78)	3.6	3.6	2.2	2.7	2.7
	1AKI	14.31	11	(4,6,75–78)	6.4	6.4	4.9	5.5	4.5
	2CDS	14.31	11	(4,6,75–78)	6.4	7.3	4.8	4.5	4.5
α-Lactalbumin human	1A4V	15.78	11	(6,77)	−2.8	−1.8	−3.8	−2.8	−2.8
Myoglobin (CO)	1DWR	16.95	11	(6,79)	−0.93	−0.93	−2.2	−0.93	−0.93
Soybean trypsin inhibitor	1AVU	19.96	9.7	(5,21,70,80)	3.6	4.6	2.5	3.4	3.6
β-Trypsin	1TPO	23.34	9.3	(5,21,81,82)	6.3	7	4.9	5.9	5.9
Trypsinogen	1TGN	23.98	9.7	(5,21,83)	−0.93	−0.83	−2.3	−1.3	−1.9
α-Chymotrypsin (mon)	4CHA	25.05	10	(5,84)	−7.2	−6.9	−8.2	−7.4	−6.9
Chymotrypsinogen A	2CGA	25.66	9.5	(5,6,85,86)	0.42	1.2	−0.74	−0.42	0.11
Carbonic anhydrase B	2CAB	28.82	8.9	(5,6,87)	2.6	3.1	1.3	1.8	2.1
Pepsin	4PEP	34.57	8.7	(21,88)	−2.6	−2.2	−3.8	−3.3	−3.1
Ovalbumin	1OVA	42.86	7.7	(6,89,90)	0	0.65	−1.1	−0.52	−0.13
Human serum albumin	1AO6	66.43	6.1	(5,21,91–93)	1.5	2.8	0.54	1.3	2.3
				RMSD	3.8	4	3.6	3.6	3.6
				mean ± SD$_{mean}$	0.92 ± 0.99	1.4 ± 1	−0.38 ± 0.96	0.38 ± 0.95	0.48 ± 0.94
Superoxide dismutase	2SOD	31.41	8.3	(5,21,94)	1.3	2.1	0.024	1.5	1.8
β-Lactoglobulin	1BEB	36.58	7.7	(5,6,95–99)	2.8	3.4	1.6	2.9	3.2
α-Chymotrypsin (dim)	4CHA	50.47	7.3	(5,86,100)	1.9	2.6	0.95	1.9	2.2
Triosephosphate isom.	1YPI	53.33	7.2	(21,101)	−1.9	−1.4	−3	−2.4	−2.1
Ricin	2AAI	61	6	(5,102)	13	14	12	13	14
Hemoglobin CO	1HCO	64.56	6.9	(6,90)	0	0.72	−0.86	−0.29	0.14
Hemoglobin oxi (human)	1GZX	64.58	7.2	(6,103)	−4.7	−4.2	−5.6	−5.3	−5.1
Citrate synthase	1CTS	97.84	5.8	(5,104)	0.34	1.4	−0.4	0	0.86
Inorganic pyrophosphatase	1FAJ	112.8	5.7	(5,105)	−6.1	−5.1	−6.8	−6.1	−5.3
G3PD apo	2GD1	143.8	5	(6,106)	0.4	1.6	−0.18	0.2	1
Holoprotein	1GD1	146.4	5.3	(6,106)	−4.5	−3.6	−5.2	−4.7	−4
LDH pig H + NAD	5LDH	148.9	5.1	(6,107)	0.59	1.6	0	0.4	0.99
Aldolase	1ADO	157.1	4.5	(5,21,108–111)	4	5.8	3.4	4	5.3
				RMSD	4.7	5	4.6	4.7	5
				mean ± SD$_{mean}$	0.55 ± 1.4	1.5 ± 1.4	−0.31 ± 1.3	0.39 ± 1.4	1 ± 1.4

The successive columns give the protein name, its PDB code, mass, and translational diffusion coefficient measured experimentally (D^t_{exp}) as well relative error of the theoretical prediction with respect to the experiment, $\Delta D_t = \left(D^t - D^t_{exp}\right)/D^t_{exp}$ (in percent). The reference experimental values are averages over the values found in the literature. Bead coverings used in the theoretical predictions include AtoB G2 and G5—grid models with base grid sizes 2 Å (G2) and 5 Å (G5) (31), SOMO and SOMO ov (overlap) model (4), HP (the atomic-shell model from HydroPro package; (53)) based on atomic resolution, and the h-atom model proposed in this work. The computational techniques include super matrix inversion (SMI) (60) and ZENO (19) (ZENO 2.3 with 1 million trajectories calculated), both implemented within the US-SOMO package (24) (US-SOMO 3087), boundary element method BEST (17) (BEST 3.9), and HYDROPRO package (HYDROPRO 10) as well as the GRPY method. The upper part of the table gives the results for monomeric proteins, and the lower part for multimeric proteins. For each part, the root mean standard deviation (RMSD) between experiment and theory is calculated averaged over different protein structures. Additionally, we calculate the mean error as well as its standard deviation. For lysozyme, we first take an average over multiple PDB structures and then use that average in the overall RMSD calculation. The symbol (n) means that structure was obtained with NMR spectroscopy.

some structures, more than one experimental measurement was reported, we take the average of respective values. The experimental results were normalized to standard conditions, and in the case of NMR experiments, H_2O-D_2O proportions were taken into account in correcting for solvent viscosity.

The numerical models were working with the protein structures taken either directly from the Protein Data Bank (PDB) or from the US-SOMO website. The latter were preferred because most of them have been already checked for gaps and corrected. Nevertheless, we have checked all of the structures for missing residues with the GapRepairer server (58) and fixed their structures with the MODELER package (59). Following Rai et al. (4), we also scanned the structures for carbohydrates and

	SOMO			SOMO ov		HP		h-atom		
GRPY	SMI	ZENO	GRPY	ZENO	GRPY	atomic	BEST	H++	ZENO	GRPY
−2.8	2.3	0.67	−0.17	−1	−2.1	−1.2	−9	1	−1	−1.5
−1.4	1.7	0.86	−0.43	−1.7	−2.4	−5.9	−5.6	−1.5	−3.4	−3.8
5.1	8.6	7.7	5.9	4.9	4.3	1.5	0.29	6.7	4.9	4.1
1.3	2.7	1.8	0.64	0	−0.55	−3.5	−3	2.1	0.91	0.091
3.6	8.2	7.3	5.6	4.5	3.5	−0.55	−2.1	5.2	2.7	2.6
3.2	8.2	7.3	5.5	3.6	2.9	−0.091	−2	5	3.6	2.5
−4	0	−0.92	−2.2	−3.7	−4.4	−9.7	−12	−3.3	−4.6	−5.4
−2.2	0.93	0	−0.93	−1.9	−2.6	−5.5	−4.1	−1.2	−2.8	−3.4
1.9	5.6	4.6	3	2.5	1.6	−1.6	−0.11	3.4	1.5	1.2
4.3	9.1	8	6.2	4.8	4.4	0.6	0.72	5.5	3.7	3.3
−2.9	1.2	0.21	−0.86	−1.9	−2.6	−5.7	−4.9	−1.3	−2.9	−3.3
−8.6	−5.8	−5.9	−7.7	−7.8	−8.7	−12	−11	−7.2	−7.8	−8.9
−1.8	1.6	1.2	−0.54	0.11	−1.6	−6.4	−4.3	−0.24	−0.95	−2.2
0.42	4.5	3.5	2.4	1.5	0.8	−1.6	−0.59	2	0.79	−0.045
−4.5	−1.5	−2.3	−3.4	−3.8	−4.6	−7.5	−10	−3.8	−5.1	−5.6
−1.7	0.39	0	−1.5	−1.6	−2.5	−4.4	−3.7	−1.4	−2.2	−3
0.28	1.3	1.3	−0.23	0.66	−0.89	−1.3	−1.1	0.54	0.66	−0.93
3.6	4.5	3.9	3.5	3.3	3.6	5.6	6.1	3.6	3.6	3.9
−1 ± 0.92	2.4 ± 1	1.6 ± 0.96	0.23 ± 0.93	−0.42 ± 0.88	−1.3 ± 0.9	−4.1 ± 1	−4.5 ± 1.1	0.22 ± 0.96	−1.1 ± 0.9	−1.9 ± 0.91
0.17	1.9	1.8	0.06	0.12	−1.2	−1.1	−1.9	0.62	−0.48	−1.2
1.6	3.4	2.8	1.5	1.5	0.4	−0.95	−0.026	2.3	1.5	0.44
0.86	3.2	2.6	1.4	1.4	0.5	−1.8	−1.4	1.9	1.2	0.41
−3.4	−1.4	−1.4	−3	−3.2	−4.2	−5.6	−5.4	−2.9	−3.9	−4.4
12	14	14	12	12	11	7.7	8	12	11	10
−1.2	1.2	0.58	−0.55	−0.58	−1.3	−2.9	−2.1	−0.17	−1	−1.7
−6.3	−3.2	−3.7	−4.7	−5.1	−5.8	−5.6	−7.7	−4.7	−5.5	−6.1
−0.86	1	0.86	−0.4	−0.34	−1.4	−3.4	−1.8	−0.19	−0.52	−1.5
−6.9	−5.6	−5.4	−6.7	−6.1	−7.4	−8.1	−8	−6.4	−6.7	−7.6
−0.5	1.4	1.8	0.28	0.4	−0.72	−2	−1.2	0.22	−0.2	−1
−5.5	−3.8	−3.6	−5	−4.7	−5.8	−6.5	−5.8	−4.9	−5.1	−6.1
−0.38	1.6	1.4	0.28	0.59	−0.36	−1.9	−1.2	0.36	0.2	−0.79
3.3	4.4	5.1	3.4	4	2.2	0.69	1.4	3.2	3.6	2.1
4.7	4.8	4.8	4.5	4.5	4.6	4.5	4.5	4.5	4.4	4.5
−0.55 ± 1.3	1.4 ± 1.4	1.3 ± 1.3	−0.11 ± 1.3	0 ± 1.3	−1.1 ± 1.3	−2.4 ± 1.1	−2.1 ± 1.2	0.1 ± 1.3	−0.45 ± 1.3	−1.3 ± 1.3

This is a continuation of Table 2.

other important ligands and added them to the bead model whenever necessary.

We compare computations performed on several different bead models: AtoB grid models with base grid sizes 2 Å (G2) and 5 Å (G5), the SOMO model, the h-atom model, and the shell model from HydroPro calculated based on atomic resolution. In the case of the AtoB and SOMO models, we perform super matrix inversion (SMI) (60) and ZENO (with 1 million trajectories) calculations in US-SOMO as well as GRPY calculations. For the h-atom model, we perform HYDRO++ calculations using the Kirkwood-Riseman approach with volume correction (case 12), ZENO (with 1 million trajectories), and GRPY. We also include results from the boundary element method implemented within the BEST program.

TABLE 3 Comparison of Intrinsic Viscosities of Different Proteins Calculated Using Various Bead Coverings and Computational Methods with the Experimental Measurements

					Relative Error $\Delta[\eta]$ (%)			
					AtoB G2			AtoB G5
Protein	PDB	Mass [kDa]	$[\eta]^{exp}[g/cm^3]$	References	SMI	ZENO	GRPY	SMI
Ribonuclease A	8RAT	13.68	3.3	(4,112)	−11	−18	−11	4.5
α-Lactalbumin (bovine)	1HFX	14.26	3.2	(5,113,114)	−4.5	−13	−4.9	13
Lysozyme	1E8L(n)	14.31	2.8	(1,5,76,115–118)	9	0.36	7.3	24
	1AKI	14.31	2.8	(1,5,76,115–118)	1.8	−6.8	0.22	19
	2CDS	14.31	2.8	(1,5,76,115–118)	0.36	−6.8	0.22	19
β-Trypsin	1TPO	23.34	3.1	(5,119)	−9	−16	−10	7.4
Trypsinogen	1TGN	23.98	3	(5,120)	2.7	−5.4	1.9	19
Chymotrypsinogen A	2CGA	25.66	3.2	(5,6,86)	−9.5	-18	−10	6.9
Carbonic anhydrase B	2CAB	28.82	2.9	(5,87,121)	1.7	−6	0.73	21
Pepsin	4PEP	34.57	3	(5,88,122)	−0.33	−8.2	−0.85	18
Ovalbumin	1OVA	42.86	3.3	(123,124)	−2.2	−10	−3	12
Human serum albumin	1AO6	66.43	4	(5,92,125–127)	−0.56	−8	−1.3	9.6
Ovotransferrin (conalbumin)	1OVT	75.41	4.2	(5,128)	−8	−16	−8.4	0.96
				RMSD	6.1	12	6.3	14
				mean ± SD_{mean}	−3.4 ± 1.6	−11 ± 1.6	−4 ± 1.6	12 ± 2.1
Superoxide dismutase	2SOD	31.41	3.3	(5,94)	4.5	−3	4.7	17
β-Lactoglobulin	1BEB	36.58	3.5	(5,129–131)	2.3	−4.2	1.3	14
Hemoglobin oxi (human)	1GZX	64.58	3.2	(6,132)	−3.8	−11	−4.5	11
Inorganic pyrophosphatase	1FAJ	112.8	3.5	(5,105)	−0.85	−9.9	−2.2	11
Lactate dehydrogenase (bovine H)	4GPD	142.9	3.8	(6,133)	−6.8	−16	−7.1	1.8
G3PD apo	2GD1	143.8	3.5	(6,134)	−0.58	−10	−1.4	11
Holoprotein	1GD1	146.4	3.5	(6,134)	−4.3	−13	−5	7.2
Aldolase	1ADO	157.1	3.7	(5,6,133,135,136)	4.1	−5.1	3.5	15
				RMSD	3.9	10	4.2	12
				mean ± SD_{mean}	−0.68 ± 1.5	−9 ± 1.6	−1.3 ± 1.5	11 ± 1.7
Cytochrome C	1HRC	12.34	2.4	(137)	28	15	24	49
Soybean trypsin inhibitor	1AVU	19.96	2.4	(5,138)	34	22	32	58
α-Chymotrypsin (mon)	4CHA	25.05	3.5	(5,84,119)	−16	−23	−16	−3.4
α-Chymotrypsin (dim)	4CHA	50.47	4.6	(5,7,84)	−31	−37	−32	−23
Citrate synthase	1CTS	97.84	4	(5,104)	−17	−24	−18	−6.6
LDH pig H + NAD	5LDH	148.9	3.8	(6,133)	−16	−24	−16	−4.7

The successive columns give the protein name, its PDB code, mass, and intrinsic viscosity measured experimentally ($[\eta]_{exp}$) as well as relative error of the theoretical prediction with respect to the experiment, $\Delta[\eta] = ([\eta] - [\eta]_{exp})/[\eta]_{exp}$ (in percent). The upper part of the table gives the results for monomeric proteins, and the central part for multimeric proteins. The lower part of the table shows the data for the proteins for which the median error over different algorithms is larger than 15% (outliers). The reference experimental values are averaged over the values found in the literature. All the other details are identical to Table 2.

Let us first discuss the translational diffusion coefficients of monomeric proteins. As seen in Table 2, the estimates of these parameters vary only slightly between all the alternative methods and bead coverings—the root mean standard deviation (RMSD) between experiments and theory averaged over different protein structures is within the 3–6% range. Nevertheless, GRPY and ZENO usually perform slightly better than the rest, with an RMSD of around 3.3–3.9% for all coverings. The SMI method gives very good results for AtoB coverings and slightly worse for the SOMO model. HydroPro and BEST perform somewhat worse, with RMSDs of 5.1 and 6.5%, respectively. For the h-atom bead model, H++, ZENO, and GRPY yield RMSDs within the 3.6–3.9% range. Still, a word of caution is in order here because experiments themselves are also subject to error, as evidenced by the different values reported by different groups. In the data in Table 2, for example, the diffusivity of α-chymotrypsin is underestimated by all the methods, whereas that of the trypsin inhibitor is overestimated. This can be related to specific characteristics of these proteins, but it can also be due to experimental inaccuracies.

For multimeric proteins, the accuracy of the predictions becomes slightly worse, with RMSDs in the 4–5% range. This can be connected to the fact that the bonds between the monomers in a multimeric protein are usually weaker than the bonds within each monomer. They are thus more prone to fluctuations, which—as noted by Aragon (23)—leads to extra viscous dissipation. This would explain why the models that

		SOMO			SOMO ov		HP		h-atom		
ZENO	GRPY	SMI	ZENO	GRPY	ZENO	GRPY	atomic	BEST	H++	ZENO	GRPY
−15	−9.1	−1.8	−18	−11	−12	−5.9	11	3.8	33	−6.1	−1.6
−9.5	−2.2	6.7	−9.5	−4.3	−6.4	0.41	16	13	38	−3.3	1.4
3.9	11	28	7.5	13	11	18	37	26	53	11	16
−3.2	4.2	9.3	−6.8	−1.4	0.36	5.2	25	24	45	3.9	8
0.36	5.4	8.6	−6.8	−0.97	3.9	7	23	23	45	3.9	8.8
−16	−8.6	−5.2	−19	−13	−13	−8.3	8.1	1.8	22	−9.7	−5.3
−2	4.4	7.1	−8.8	−2.1	−2	3.6	21	11	36	1.4	6
−15	−7.2	−1.3	−18	−10	−12	−7.3	14	0.34	17	−12	−5.4
−2.5	3.6	8.3	−9.4	−2	−2.5	3.1	16	7.4	35	−2.5	6
−4.9	1.8	6.6	−8.2	−1.7	−1.6	2.5	18	22	43	1.6	5.9
−7	−1.3	6.5	−7	−1.8	−4	1.5	13	4.8	44	−0.98	3.3
−5.5	−0.34	11	−5.5	1.5	−3	3.7	11	4.1	31	−3	4
−13	−8.1	−2.4	−13	−8.7	−11	−5.5	6.7	−2.9	37	−11	−4.4
9.9	5.7	7.6	12	6.8	7.9	5.5	16	12	36	6.5	5.5
−8.2 ± 1.8	−1.8 ± 1.7	4.6 ± 1.9	−11 ± 1.7	−4.5 ± 1.7	−5.7 ± 1.7	−0.21 ± 1.7	15 ± 1.9	8.2 ± 2.6	35 ± 2.8	−3.6 ± 1.7	1.9 ± 1.6
−3	4.7	14	−3	5.2	3	9.5	15	12	57	3	9.8
−4.2	1.5	11	−4.2	2	1.4	5.7	15	6.6	54	−1.4	5.8
−8.2	−2.3	0.32	−15	−7.1	−8.2	−3.3	0.89	2.5	24	−8.2	−2.1
−9.9	−1.6	6.2	−9.9	−2.1	−7	0.2	12	6.1	32	−1.4	5.2
−13	−7.2	−1.6	−13	−7.8	−11	−4.9	3.3	−5.3	15	−11	−4.4
−7.2	−0.23	3.8	−10	−2.4	−4.3	0.78	10	1.9	23	−4.3	1.9
−10	−4	0.29	−13	−5.4	−10	−2.8	4.4	−3.1	19	−7.2	−1.7
−2.4	4.1	10	−2.4	4	0.27	7.7	18	9.8	31	3	8.1
8.1	3.8	7.7	10	5	6.8	5.3	11	6.8	35	5.9	5.6
−7.2 ± 1.3	−0.63 ± 1.4	5.5 ± 2	−8.8 ± 1.7	−1.7 ± 1.8	−4.5 ± 1.9	1.6 ± 1.9	9.8 ± 2.2	3.8 ± 2.1	32 ± 5.5	−3.4 ± 1.8	2.8 ± 1.8
19	28	32	11	18	19	26	30	56	63	19	24
22	34	44	22	31	30	36	58	43	75	30	38
−20	−15	−9.4	−23	−17	−20	−14	2.4	−7.6	7.4	−18	−13
−37	−32	−28	−37	−33	−35	−31	−22	−27	−9	−35	−31
−22	−16	−11	−22	−17	−19	−15	−5	−14	13	−19	−14
−21	−15	−8.9	−24	−17	−21	−15	−6.7	−13	13	−18	−14

This is a continuation of Table 3.

work accurately for monomers tend to overpredict diffusivities in multimeric proteins. One possible way of accounting for this is to increase the hydration layer for multimeric proteins (because, as elucidated in (23,51,52) the hydration layer is an effective way of taking into account extra viscous-energy dissipation due to the dynamic fluctuations of the positions of the surface atoms). However, we are not exploring these issues here, leaving them for further study.

For intrinsic viscosity (Table 3), the differences between the methods become more notable. Here, for all bead coverings, the GRPY method performs the most consistently, yielding an RMSD of 5.5–6.8% for monomeric proteins and 3.8–5.6% for multimeric structures. The SMI method for AtoB G2 covering also produces very good results, with RMSDs of 6.1 and 3.9%, respectively. Interestingly, for intrinsic viscosity, the agreement with the experiment for multimeric proteins is not worse than that for monomeric proteins, unlike the case of translational diffusion.

Importantly, there is a group of proteins (cf. the *bottom part* of Table 4) for which all of the existing methods fail, producing relative errors of 20–70%. Moreover, even if one of the methods gives results reasonably close to the experiment for some of these proteins, it fails for other proteins from this group, which makes it hard to indicate a clear leader. These discrepancies could be connected with the experimental errors, or they may indicate that, for these proteins, some of the important factors are missing in theoretical models. We separate out these outliers, adopting the

TABLE 4 Comparison of Rotational Correlation Times of Different Proteins Calculated Using Various Bead Coverings and Computational Methods with the Experimental Measurements

					Relative Error $\Delta[\tau_c]$ (%)										
					AtoB G2		AtoB G5		SOMO		SOMO ov	HP		h-atom	
Name	PDB	Mass [kDa]	τ_c^{exp}[ns]	References	SMI	GRPY	SMI	GRPY	SMI	GRPY	GRPY	atomic	BEST	H++	GRPY
Calbindin-D9k holoprotein	2BCB (n)	8.445	4.9	(6,139–141)	−5.3	−7.3	6.8	−2.9	2.6	−10	−6.4	8.2	−3.4	1.8e+02	−8.5
Apo	1CLB (n)	8.462	4.9	(6,139–141)	−2.7	−5.3	6.4	−2.7	4.4	−8.1	−4.3	7.6	−0.79	1.8e+02	−5.5
Ubiquitin	1UBQ	8.566	4.6	(6,142–144)	11	8.2	28	12	17	2.6	9.2	24	13	2.1e+02	9.8
Cytochrome b5	1NX7 (n)	10.06	5.6	(6,145)	−8	−10	0.35	−8.9	−4.1	−13	−8.5	9.3	−5.3	1.7e+02	−9.3
Staphylococcal nuclease SN-OB	2SOB (n)	11.61	10	(6,146,147)	−17	−18	−11	−18	−9	−18	−15	−5.5	−6.2	1.1e+02	−15
Ribonuclease A	8RAT	13.68	8	(4,148,149)	−8.5	−10	4.1	−8.7	−2.3	−11	−6.8	8.8	2.1	1.6e+02	−2.9
Lysozyme	1E8L (n)	14.31	7.6	(6,61,150,151)	2.7	0.9	14	4.1	17	4.9	7.6	23	15	1.7e+02	5.4
	2CDS	14.31	7.6	(6,61,150,151)	−6	−7.3	9.2	−2.7	−0.65	−9.5	−3.5	9.8	11	1.6e+02	−2.7
	1AKI	14.31	7.6	(6,61,150,151)	−5.5	−7.6	8.9	−4.1	−0.39	−10	−5.2	12	11	1.6e+02	−3.4
Staphylococcal nuclease SN	1STN	16.81	13	(6,146,147)	9.7	8.6	20	9.2	16	7.4	13	25	20	1.6e+02	14
Myoglobin (CO)	1DWR	16.95	10	(6,152,153)	−1.9	−3.8	8.8	−4.2	1.3	−8.6	−4.8	8.7	−0.99	1.8e+02	−2.5
Interleukin-1β	6I1B (n)	17.38	12	(6,154)	−8.6	−10	2.3	−9.8	−3	−12	−9.9	9.1	−5.8	1.3e+02	−14
Leukemia inhibition factor	1A7M (n)	19.8	13	(6,61,155,156)	−8.6	−9.4	0.53	−8.5	−1.2	−10	−7.3	15	2.8	1.3e+02	−5.3
	1LKI	19.8	13	(6,61,155,156)	−8.6	−10	3.4	−8.3	1.3	−8.1	−5.4	16	3.2	1.4e+02	−0.98
HIV-1 protease + DMP323	1BVG (n)	21.49	13	(6,61,62,157)	−5.4	−6.8	4.1	−5.7	2.9	−6.3	−3.5	12	1.8	1.5e+02	−5.9
Trp repressor	1WRT (n)	23.79	22	(6,61,158)	−3.4	−4.1	6	−1.3	10	−1.3	0.98	24	11	1.2e+02	2.5
Savinase	1SVN	26.7	12	(6,61,159)	−2.4	−3.8	13	−2.3	−1.6	−9	−5.6	11	3.8	1.7e+02	−1.2
N-terminal domain of enzyme I	2EZA (n)	28.35	21	(62)	11	10	21	10	25	11	14	24	14	1.7e+02	11
Hemoglobin oxi (human)	1GZX	64.58	35	(6,160) (DS)	−3.8	−5.3	8.5	−3.6	−1.4	−8.7	−5.8	−2.3	−0.4	1.6e+02	−4.9
				RMSD	8.5	9.3	12	8.5	9.7	11	8.8	15	8.6	1.6e+02	8.9
				mean ± SD_{mean}	−3.5 ± 2	−5.1 ± 2	7.9 ± 2.3	−3.3 ± 2	3.3 ± 2.4	−6.9 ± 2.1	−3 ± 2.1	12 ± 2.2	3.4 ± 2	1.6e+02 ± 6	−2.7 ± 2.2
Eglin c	1EGL (n)	8.092	6.1	(6,161)	−18	−19	−13	−21	−8.8	−20	−18	−1.4	−9.2	1.3e+02	−13
Barstar C40/82A	1BTA (n)	10.21	6.9	(6,162,163)	−15	−17	−4.4	−15	−8	−19	−17	1.1	−18	1.3e+02	−21
Cytochrome b5	1HKO (n)	12.39	5.6	(6,145)	76	74	88	72	97	79	83	1.2e+02	90	3.2e+02	76
α-Lactalbumin (bovine)	1HFX	14.26	10	(6,164) (FD) (6,165) (FD, FC)	−23	−24	−12	−23	−17	−25	−23	−13	−14	1.1e+02	−23
Hemoglobin horse oxi	1G0B	32.41	40	(6,160) (DS)	−55	−56	−50	−56	−54	−58	−56	−49	−55	12	−56
β-Lactoglobulin	1BEB	36.58	11	(6,166) (DD) (6,167) (FD)	1.2e+02	1.1e+02	1.4e+02	1.1e+02	1.3e+02	1.1e+02	1.2e+02	1.4e+02	1.2e+02	4.6e+02	1.2e+02
Ovalbumin	1OVA	42.86	21	(6,103) (EB)	18	16	33	18	27	17	20	33	23	2.1e+02	22

The successive columns give the protein name, its PDB code, mass, and rotational relaxation measured experimentally (τ_c^{exp}) as well as relative error of the theoretical prediction with respect to the experiment, $\Delta\tau_c = (\tau_c - \tau_c^{exp})/\tau_c^{exp}$ (in percent). The reference experimental values are averages over the values found in the literature. The lower part of the table shows the data for the proteins for which the median error over different algorithms is larger than 15%. All the other details are identical to Table 2. The (n) symbol denotes structures determined using NMR spectroscopy. The experimental data on rotational relaxation times was obtained with NMR techniques unless otherwise specified. Other experimental methods include electric birefringence (EB), fluorescence polarization (FP), dielectric dispersion (DS), and decay of dichroism (DD). For an extensive review of NMR relaxation methods and experiments, please refer to (168).

criterion that the median error over different algorithms in an outlier should be larger than 15%.

Next, in Table 4, we present the data on rotational relaxation times. Following (61), we define the rotational correlation time τ_c as the inverse of the average of the frequencies f_j, $j = 1,...,5$, defined in Eq. C1:

$$(\tau_c)^{-1} = \frac{1}{5}\sum_{j=1}^{5} f_j. \tag{32}$$

Again, we separate the outliers for which the median error over different algorithms is larger than 15%. For the rest of the structures, the best performing methods are GRPY (for h-atom, AtoB G5, and SOMO with overlaps), SMI in US-SOMO for G2 bead covering, and BEST.

A word of caution is in order here. Although most of the data in Table 4 has been measured using NMR techniques, which are capable of fully determining the rotational diffusion tensor (62), other techniques, such as electric birefringence or fluorescent polarization, do not give direct access to all eigenvalues of D^r. The estimation of τ_c relies then on various approximations or additional assumptions about the shape of the molecule, which might introduce errors (see the discussion of these issues in (63)).

Finally, in Table 5, we provide data on the computational efficiency of the GRPY method along with the information on hardware used. We report CPU time and memory usage for four different protein structures of increasing complexity with the bead models produced by h-atom. The GRPY method consumes a relatively large amount of memory because it performs Cholesky decomposition of an $11N \times 11N$ dense matrix, with N standing for the number of beads in the model.

CONCLUSION

Reformulation of the Rotne-Prager-Yamakawa approximation using the integral formalism (Eq. 15) leads to a robust numerical scheme capable of calculation of hydrodynamic properties of macromolecules represented as a collection of beads of different radii both overlapping and nonoverlapping. In general, the method performs better than the existing bead models because of the inclusion of the larger number of force and velocity multipoles. In particular, because of the incorporation of the dipolar components of the hydrodynamic interaction tensors, the intrinsic viscosity of macromolecules is calculated directly, without a need for any correction factors.

Software availability

The source code and precompiled versions of the GRPY program for Windows and Linux operating systems are available for download from github repository https://github.com/pjzuk/GRPY, with Zenodo-listed release DOI 10.5281/zenodo.1325126, and from http://www.fuw.edu.pl/~piotrek/sofware. They can be downloaded and used under GNU General Public License version 3.

APPENDIX A: GRAND FRICTION MATRIX OF THE MACROMOLECULE

In this Appendix, we present the derivation of Eq. 6 between the grand friction matrix of the macromolecule $\boldsymbol{\zeta}_c$ and the N-body grand friction matrix $\boldsymbol{\zeta}_N$. To this end, we envisage that the molecule is immersed in an external linear flow,

$$\boldsymbol{v}_\infty(\boldsymbol{r}) = \boldsymbol{E}_c \cdot (\boldsymbol{r} - \boldsymbol{R}_0), \tag{A1}$$

where $\boldsymbol{E}_c$ is a symmetric velocity gradient matrix. When the macromolecule moves as a rigid body, the translational and rotational velocities of individual constituents ($\boldsymbol{U}_i$, $\boldsymbol{\Omega}_i$) are linked with those of a body as a whole ($\boldsymbol{U}_c$, $\boldsymbol{\Omega}_c$) in the following way:

$$\begin{aligned} \boldsymbol{U}_i &= \boldsymbol{U}_c + \boldsymbol{\Omega}_c \times (\boldsymbol{R}_i - \boldsymbol{R}_0), \\ \boldsymbol{\Omega}_i &= \boldsymbol{\Omega}_c, \\ \boldsymbol{E}_{\infty,i} &= \boldsymbol{E}_c, \end{aligned} \tag{A2}$$

where $\boldsymbol{R}_0$ is the reference point with respect to which the translation and rotation are defined. Eq. A2 allow us to express the vector in the right hand side of Eq. 3 as

$$\begin{pmatrix} \boldsymbol{E}_c \cdot (\tilde{\boldsymbol{R}} - \boldsymbol{R}_0) - \tilde{\boldsymbol{U}} \\ -\tilde{\boldsymbol{\Omega}} \\ \tilde{\boldsymbol{E}}_c \end{pmatrix} = \boldsymbol{T}_N(\boldsymbol{R}_0) \cdot \begin{pmatrix} -\boldsymbol{U}_c \\ -\boldsymbol{\Omega}_c \\ \boldsymbol{E}_c \end{pmatrix}, \tag{A3}$$

where $\tilde{\boldsymbol{R}} = (\boldsymbol{R}_1, \boldsymbol{R}_2, \ldots, \boldsymbol{R}_N)$ and $\boldsymbol{T}_N$ is an $11N \times 11$ matrix. In the above, we made use of the fact that the external flow of the form given by Eq. A1 vanishes at $\boldsymbol{R}_0$. Similarly, $\boldsymbol{\omega}_\infty$ also vanishes because the gradient of $\boldsymbol{v}_\infty$ is symmetric.

The relation between $\boldsymbol{\zeta}_c$ and the N-body grand friction matrix $\boldsymbol{\zeta}_N$ can then be cast in the form

$$\boldsymbol{\zeta}_c = \boldsymbol{T}_N(\boldsymbol{R}_0)^T \cdot \boldsymbol{\zeta}_N \cdot \boldsymbol{T}_N(\boldsymbol{R}_0), \tag{A4}$$

with $\boldsymbol{T}_N$ defined in Eq. A3.

TABLE 5 Performance of the GRPY Program

				Serial GRPY		Parallel GRPY 1 core		Parallel GRPY 32 cores	
Protein	PDB	Mass (kDa)	Bead number	execution time	memory	execution time	memory	execution time	memory
Cytochrome C	1HRC	12.34	601	2 m 32 s	0.6 GB	2 m 20 s	1.3 GB	10 s	1.3 GB
β-trypsin	1TPO	23.34	993	11 m 12 s	1.6 GB	10 m 19 s	3.5 GB	35 s	3.5 GB
Hemoglobin CO	1HCO	64.56	3072	5 h 05 m 36 s	15 GB	4 h 35 m 59 s	33.5 GB	11 m 32 s	33.5 GB
Inorganic pyrophosphatase	1FAJ	112.8	5058	24 h 39 m 03 s	42.4 GB	23 h 11 m 53 s	90.7 GB	50 m 44 s	90.7 GB

Program execution time and Random Access Memory usage in gigabytes (GB) calculating the hydrodynamic properties of h-atom models of proteins. Program was executed on the computer with four Intel Xeon Central Processing Units E5-4620 v2 at 2.60 GHz with the total number of 32 cores and 264 gigabytes Random Access Memory with Scientific Linux 7.4.

APPENDIX B: TIME DEPENDENCE OF MEAN-SQUARE DISPLACEMENT

Here, we briefly summarize the results of (41) concerning the time dependence of the mean-square displacement of an arbitrary point of a macromolecule. The latter can be shown to be

$$\begin{aligned}\left\langle \left(\boldsymbol{R}(t)-\boldsymbol{R}(0)\right)^2\right\rangle &= 6D_l^t + 2(k_{\mathrm{B}}T)^2 \\ &\times \left[\left(\frac{\mu_{23}^{rt}-\mu_{32}^{rt}}{D_2^r+D_3^r}\right)^2\left(1-e^{-\left(D_2^r+D_3^r\right)t}\right)\right. \\ &+\left(\frac{\mu_{31}^{rt}-\mu_{13}^{rt}}{D_1^r+D_3^r}\right)^2\left(1-e^{-\left(D_1^r+D_3^r\right)t}\right) \\ &\left.+\left(\frac{\mu_{12}^{rt}-\mu_{21}^{rt}}{D_1^r+D_2^r}\right)^2\left(1-e^{-\left(D_1^r+D_2^r\right)t}\right)\right].\end{aligned} \tag{B1}$$

In the above, the indices 1,2,3 denote base vectors in linear space in which $\boldsymbol{D}^r$ (Eq. 8) is diagonal. As observed, if $\boldsymbol{R}_0$ is chosen in such a way as to guarantee that the tensor $\boldsymbol{\mu}^{rt}$ is symmetric, i.e., $\mu_{ij}^{rt}=\mu_{ji}^{rt}$, then the mean-square displacement is linear in time. The point with above properties is the so-called mobility center of a molecule. If the tracked point is not a mobility center, then three decaying exponential modes appear with the respective relaxation times given by Eq. 18.

APPENDIX C: BROWNIAN CONTRIBUTION TO THE INTRINSIC VISCOSITY

In Eq. 26 for the Brownian contribution to the intrinsic viscosity, five characteristic frequencies f_j appear. The explicit formulas for these frequencies read as follows (42,43):

$$\begin{aligned} f_1 &= 6D^r + 2\Delta, \\ f_2 &= 6D^r - 2\Delta, \\ f_3 &= 3\left(D^r + D_1^r\right), \\ f_4 &= 3\left(D^r + D_2^r\right), \\ f_5 &= 3\left(D^r + D_3^r\right), \end{aligned} \tag{C1}$$

where

$$D^r = \frac{1}{3}\mathrm{Tr}\boldsymbol{D}^r = \frac{1}{3}\left(D_1^r + D_2^r + D_3^r\right)$$

$$\Delta = \left(\left(D_1^r\right)^2 + \left(D_2^r\right)^2 + \left(D_3^r\right)^2 - D_1^rD_2^r - D_2^rD_3^r - D_1^rD_3^r\right)^{1/2}.$$

On the other hand, the parameters A_i, which give the weights of successive modes to the Brownian viscosity (Eq. 26), read as follows:

$$\begin{aligned} A_3 &= 2H_{23}^2, \quad A_4 = 2H_{31}^2, \quad A_5 = 2H_{12}^2, \\ H_{23} &= \mu_{133}^{rd} - \mu_{313}^{rd} + \mu_{212}^{rd} - \mu_{122}^{rd}, \\ H_{31} &= \mu_{211}^{rd} - \mu_{121}^{rd} + \mu_{323}^{rd} - \mu_{233}^{rd}, \\ H_{12} &= \mu_{322}^{rd} - \mu_{232}^{rd} + \mu_{131}^{rd} - \mu_{311}^{rd}, \\ A_1 + A_2 &= H_{11}^2 + H_{22}^2 + H_{33}^2, \\ A_1 - A_2 &= \frac{1}{\Delta}\left[\overline{c}_1D_1^r + \overline{c}_2D_2^r + \overline{c}_3D_3^r\right], \end{aligned} \tag{C2}$$

with

$$\begin{aligned} \overline{c}_1 &= -2H_{11}^2 + H_{22}^2 + H_{33}^2, \\ \overline{c}_2 &= H_{11}^2 - 2H_{22}^2 + H_{33}^2, \\ \overline{c}_3 &= H_{11}^2 + H_{22}^2 - 2H_{33}^2, \\ H_{11} &= 2\left(\mu_{321}^{rd} - \mu_{231}^{rd}\right), \\ H_{22} &= 2\left(\mu_{132}^{rd} - \mu_{312}^{rd}\right), \\ H_{33} &= 2\left(\mu_{231}^{rd} - \mu_{123}^{rd}\right). \end{aligned} \tag{C3}$$

SUPPORTING MATERIAL

One data file is available at http://www.biophysj.org/biophysj/supplemental/S0006-3495(18)30824-5.

AUTHOR CONTRIBUTIONS

P.J.Z., B.C., and P.S. designed research, performed research, analyzed data and wrote the manuscript. P.J.Z. wrote and tested the GRPY program.

ACKNOWLEDGMENTS

Constructive and insightful comments from anonymous referees are gratefully acknowledged. The authors acknowledge Srishti Nayak's editorial help in preparing this manuscript.

P.J.Z. would like to acknowledge the support of the National Science Centre (grant no. 2013/09/N/ST3/04308).

SUPPORTING CITATIONS

References (64–67) appear in the Supporting Material.

REFERENCES

1. Harding, S. E. 1997. The intrinsic viscosity of biological macromolecules. Progress in measurement, interpretation and application to structure in dilute solution. *Prog. Biophys. Mol. Biol.* 68:207–262.
2. Bloomfield, V. A. 2000. Survey of biomolecular hydrodynamics. *In* On-Line Biophysics Textbook: Separations and Hydrodynamics. T. M. Schuster, ed. Biophysics Society.
3. Byron, O. 2000. Hydrodynamic bead modeling of biological macromolecules. *Methods Enzymol.* 321:278–304.
4. Rai, N., M. Nöllmann, …, M. Rocco. 2005. SOMO (SOlution MOdeler) differences between X-Ray- and NMR-derived bead models suggest a role for side chain flexibility in protein hydrodynamics. *Structure.* 13:723–734.
5. Hahn, D. K., and S. R. Aragon. 2006. Intrinsic viscosity of proteins and platonic solids by boundary element methods. *J. Chem. Theory Comput.* 2:1416–1428.
6. Brookes, E., B. Demeler, …, M. Rocco. 2010. The implementation of SOMO (SOlution MOdeller) in the UltraScan analytical ultracentrifugation data analysis suite: enhanced capabilities allow the reliable hydrodynamic modeling of virtually any kind of biomacromolecule. *Eur. Biophys. J.* 39:423–435.
7. Aragon, S. R. 2011. Recent advances in macromolecular hydrodynamic modeling. *Methods.* 54:101–114.
8. Echiyama, S., F. Arisaka, …, T. Laue. 2016. Analytical Ultracentrifugation: Instrumentation, Software, and Applications. Springer, Tokyo, Japan.

9. Jeffery, G. B. 1922. The motion of ellipsoidal particles immersed in a viscous fluid. *Proc. R. Soc. Lond. A Math. Phys. Sci.* 102:161–179.
10. Simha, R. 1940. The influence of Brownian movement on the viscosity of solutions. *J. Phys. Chem.* 44:25–34.
11. Brenner, H. 1974. Rheology of a dilute suspension of axisymmetric Brownian particles. *Int. J. Multiph. Flow.* 1:195–341.
12. Harding, S. E., M. Dampier, and A. J. Rowe. 1982. The viscosity increment for ellipsoids of revolution. Some observations on the Simha formula. *Biophys. Chem.* 15:205–208.
13. Bloomfield, V., W. O. Dalton, and K. E. Van Holde. 1967. Frictional coefficients of multisubunit structures. I. Theory. *Biopolymers.* 5:135–148.
14. de la Torre, J. G., and V. A. Bloomfield. 1978. Hydrodynamic properties of macromolecular complexes. IV. Intrinsic viscosity theory, with applications to once-broken rods and multisubunit proteins. *Biopolymers.* 17:1605–1627.
15. Byron, O. 2008. Hydrodynamic modeling: the solution conformation of macromolecules and their complexes. *Methods Cell Biol.* 84:327–373.
16. Allison, S. A. 1999. Low Reynolds number transport properties of axisymmetric particles employing stick and slip boundary conditions. *Macromolecules.* 32:5304–5312.
17. Aragon, S. 2004. A precise boundary element method for macromolecular transport properties. *J. Comput. Chem.* 25:1191–1205.
18. Kang, E. H., M. L. Mansfield, and J. F. Douglas. 2004. Numerical path integration technique for the calculation of transport properties of proteins. *Phys. Rev. E Stat. Nonlin. Soft Matter Phys.* 69:031918.
19. Mansfield, M. L., and J. F. Douglas. 2008. Improved path integration method for estimating the intrinsic viscosity of arbitrarily shaped particles. *Phys. Rev. E Stat. Nonlin. Soft Matter Phys.* 78:046712.
20. Juba, D., D. J. Audus, …, W. Keyrouz. 2017. ZENO: software for calculating hydrodynamic, electrical, and shape properties of polymer and particle suspensions. *J. Res. Natl. Inst. Stand. Technol.* 122:20.
21. Rocco, M., and O. Byron. 2015. Computing translational diffusion and sedimentation coefficients: an evaluation of experimental data and programs. *Eur. Biophys. J.* 44:417–431.
22. de la Torre, J. G. 2016. The HYDRO software suite for the prediction of solution properties of rigid and flexible macromolecules and nanoparticles. Analytical Ultracentrifugation: Instrumentation, Software, and Applications. Springer, pp. 195–217.
23. Aragon, S. R. 2016. Accurate hydrodynamic modeling with the boundary element method. Analytical Ultracentrifugation: Instrumentation, Software, and Applications. Springer, pp. 219–247.
24. Brookes, E., and M. Rocco. 2016. Calculation of hydrodynamic parameters: US-SOMO. Analytical Ultracentrifugation: Instrumentation, Software, and Applications. Springer, pp. 169–193.
25. Byron, O. 2016. Introduction: calculation of hydrodynamic parameters. Analytical Ultracentrifugation: Instrumentation, Software, and Applications. Springer, pp. 147–167.
26. Youngren, G., and A. Acrivos. 1975. Stokes flow past a particle of arbitrary shape: a numerical method of solution. *J. Fluid Mech.* 69:377–403.
27. Pozrikidis, C. 1992. Boundary Integral and Singularity Methods for Linearized Viscous Flow. Cambridge University Press, Cambridge, UK.
28. Garcia de la Torre, J., S. Navarro, …, J. J. Lopez Cascales. 1994. HYDRO: a computer program for the prediction of hydrodynamic properties of macromolecules. *Biophys. J.* 67:530–531.
29. de la Torre, J. G., Gdel. R. Echenique, and A. Ortega. 2007. Improved calculation of rotational diffusion and intrinsic viscosity of bead models for macromolecules and nanoparticles. *J. Phys. Chem. B.* 111:955–961.
30. de la Torre, J. G., and B. Carrasco. 1998. Intrinsic viscosity and rotational diffusion of bead models for rigid macromolecules and bioparticles. *Eur. Biophys. J.* 27:549–557.
31. Byron, O. 1997. Construction of hydrodynamic bead models from high-resolution X-ray crystallographic or nuclear magnetic resonance data. *Biophys. J.* 72:408–415.
32. García De La Torre, J., M. L. Huertas, and B. Carrasco. 2000. Calculation of hydrodynamic properties of globular proteins from their atomic-level structure. *Biophys. J.* 78:719–730.
33. Zipper, P., and H. Durchschlag. 1997. Calculation of hydrodynamic parameters of proteins from crystallographic data using multibody approaches. *Prog. Colloid Polym. Sci.* 107:58–71.
34. Zuk, P., E. Wajnryb, …, P. Szymczak. 2014. Rotne-Prager-Yamakawa approximation for different-sized particles in application to macromolecular bead models. *J. Fluid Mech.* 741:R5.
35. Wajnryb, E., K. A. Mizerski, …, P. Szymczak. 2013. Generalization of the Rotne–Prager–Yamakawa mobility and shear disturbance tensors. *J. Fluid Mech.* 731:R3.
36. Zuk, P. J., B. Cichocki, and P. Szymczak. 2017. Intrinsic viscosity of macromolecules within the generalized Rotne–Prager–Yamakawa approximation. *J. Fluid Mech.* 822:R2.
37. Kim, S., and S. J. Karrila. 1991. Microhydrodynamics: Principles and Selected Applications. Butterworth-Heinemann, London, UK.
38. Durlofsky, L., J. F. Brady, and G. Bossis. 1987. Dynamic simulation of hydrodynamically interacting particles. *J. Fluid Mech.* 180:21–49.
39. Brady, J., and G. Bossis. 1988. Stokesian dynamics. *Annu. Rev. Fluid Mech.* 20:111–157.
40. Goldstein, R. F. 1985. Macromolecular diffusion constants: a calculational strategy. *J. Chem. Phys.* 83:2390–2397.
41. Cichocki, B., M. L. Ekiel-Jeżewska, and E. Wajnryb. 2012. Communication: translational Brownian motion for particles of arbitrary shape. *J. Chem. Phys.* 136:071102.
42. Rallison, J. 1978. The effects of Brownian rotations in a dilute suspension of rigid particles of arbitrary shape. *J. Fluid Mech.* 84:237–263.
43. Cichocki, B., M. Ekiel-Jezewska, and E. Wajnryb. 2012. Intrinsic viscosity for Brownian particles of arbitrary shape. *J. Phys. Conf. Ser.* 392:012004.
44. Mazur, P., and W. van Saarloos. 1982. Many-sphere hydrodynamic interactions and mobilities in a suspension. *Physica A.* 115:21–57.
45. Felderhof, B. U. 1988. Many-body hydrodynamic interactions in suspensions. *Physica A.* 151:1–16.
46. Cichocki, B., B. U. Felderhof, …, J. Bławzdziewicz. 1994. Friction and mobility of many spheres in Stokes flow. *J. Chem. Phys.* 100:3780–3790.
47. Ekiel-Jeżewska, M., and E. Wajnryb. 2009. Precise multipole method for calculating hydrodynamic interactions between spherical particles in the Stokes flow. *In* Theoretical Methods for Micro Scale Viscous Flows. F. Feuillebois and A. Sellier, eds. Transworld Research Network, pp. 127–172.
48. Douglas, J. F., and E. J. Garboczi. 1995. Intrinsic viscosity and the polarizability of particles having a wide range of shapes. *Adv. Chem. Phys.* 91:85–154.
49. Yamakawa, H. 1971. Modern Theory of Polymer Solutions. Harper & Row, New York.
50. Wüthrich, K., M. Billeter, …, G. Wider. 1996. NMR studies of the hydration of biological macromolecules. *Faraday Discuss.* 103: 245–253.
51. Halle, B., and M. Davidovic. 2003. Biomolecular hydration: from water dynamics to hydrodynamics. *Proc. Natl. Acad. Sci. USA.* 100:12135–12140.
52. Zhang, L., L. Wang, …, D. Zhong. 2007. Mapping hydration dynamics around a protein surface. *Proc. Natl. Acad. Sci. USA.* 104:18461–18466.
53. Ortega, A., D. Amorós, and J. García de la Torre. 2011. Prediction of hydrodynamic and other solution properties of rigid proteins from atomic- and residue-level models. *Biophys. J.* 101:892–898.
54. Kuntz, I., Jr., and W. Kauzmann. 1974. Hydration of proteins and polypeptides. *Adv. Protein Chem.* 28:239–345.

55. Gerstein, M., and C. Chothia. 1996. Packing at the protein-water interface. *Proc. Natl. Acad. Sci. USA.* 93:10167–10172.

56. Sanner, M. F., A. J. Olson, and J. C. Spehner. 1996. Reduced surface: an efficient way to compute molecular surfaces. *Biopolymers.* 38:305–320.

57. Venable, R. M., and R. W. Pastor. 1988. Frictional models for stochastic simulations of proteins. *Biopolymers.* 27:1001–1014.

58. Jarmolinska, A. I., M. Kadlof, …, J. I. Sulkowska. 2018. GapRepairer - a server to model a structural gap and validate it using topological analysis. *Bioinformatics.* 1:8.

59. Eswar, N., B. Webb, …, A. Sali. 2006. Comparative protein structure modeling using Modeller. *Curr. Protoc. Bioinformatics.* Chapter 5:Unit 5.6.

60. Garcia de la Torre, J. G., and V. A. Bloomfield. 1981. Hydrodynamic properties of complex, rigid, biological macromolecules: theory and applications. *Q. Rev. Biophys.* 14:81–139.

61. García de la Torre, J., M. L. Huertas, and B. Carrasco. 2000. HYDRONMR: prediction of NMR relaxation of globular proteins from atomic-level structures and hydrodynamic calculations. *J. Magn. Reson.* 147:138–146.

62. Clore, G. M., A. M. Gronenborn, …, N. Tjandra. 1998. Determining the magnitude of the fully asymmetric diffusion tensor from heteronuclear relaxation data in the absence of structural information. *J. Am. Chem. Soc.* 120:4889–4890.

63. Aragon, S., and D. K. Hahn. 2006. Precise boundary element computation of protein transport properties: diffusion tensors, specific volume, and hydration. *Biophys. J.* 91:1591–1603.

64. Schlecht, P., H. Vogel, and A. Mayer. 1968. Effect of oxygen binding on the dielectric properties of hemoglobin. *Biopolymers.* 6:1717–1725.

65. Brookes, E., B. Demeler, and M. Rocco. 2010. Developments in the US-SOMO bead modeling suite: new features in the direct residue-to-bead method, improved grid routines, and influence of accessible surface area screening. *Macromol. Biosci.* 10:746–753.

66. Anderson, E., Z. Bai, …, D. Sorensen. 1999. LAPACK Users' Guide. SIAM, Philadelphia, PA.

67. Agullo, E., J. Dongarra, …, A. YarKhan. 2009. PLASMA Users' Guide. Technical Report http://icl.cs.utk.edu/projectsfiles/plasma/pdf/users_guide.pdf.

68. Fling, M., N. H. Horowitz, and S. F. Heinemann. 1963. The isolation and properties of crystalline tyrosinase from Neurospora. *J. Biol. Chem.* 238:2045–2053.

69. Larew, L. A., and R. R. Walters. 1987. A kinetic, chromatographic method for studying protein hydrodynamic behavior. *Anal. Biochem.* 164:537–546.

70. Walters, R. R., J. F. Graham, …, D. J. Anderson. 1984. Protein diffusion coefficient measurements by laminar flow analysis: method and applications. *Anal. Biochem.* 140:190–195.

71. Atlas, S. M., and E. Farber. 1956. On the molecular weight of cytochrome c from mammalian heart muscle. *J. Biol. Chem.* 219:31–37.

72. Clark, S. M., D. G. Leaist, and L. Konermann. 2002. Taylor dispersion monitored by electrospray mass spectrometry: a novel approach for studying diffusion in solution. *Rapid Commun. Mass Spectrom.* 16:1454–1462.

73. Polson, A. 1939. Über die berechnung der gestalt von proteinmolekülen. *Colloid Polym. Sci.* 88:51–61.

74. Gordon, W. G., and W. F. Semmett. 1953. Isolation of crystalline α-lactalbumin from Milk2. *J. Am. Chem. Soc.* 75:328–330.

75. Dubin, S. B., N. A. Clark, and G. B. Benedek. 1971. Measurement of the rotational diffusion coefficient of lysozyme by depolarized light scattering: configuration of lysozyme in solution. *J. Chem. Phys.* 54:5158–5164.

76. Sophianopoulos, A. J., C. K. Rhodes, …, K. E. Van Holde. 1962. Physical studies of lysozyme. I. Characterization. *J. Biol. Chem.* 237:1107–1112.

77. Barel, A. O., J. P. Prieels, …, J. Léonis. 1972. Comparative physicochemical studies of human alpha-lactalbumin and human lysozyme. *Biochim. Biophys. Acta.* 257:288–296.

78. Luzzati, A., and M. Champagne. 1957. Masse moléculaire et dimensions de la molécule de lysozyme en solution. *Cr. Hebd. Acad. Sci.* 244:2930–2932.

79. Ehrenberg, A. 1957. Determination of molecular weights and diffusion coefficients in the ultracentrifuge. *Acta Chem. Scand.* 11:1257–1270.

80. Rackis, J. J., H. A. Sasame, …, A. K. Smith. 1962. Soybean trypsin inhibitors: isolation, purification and physical properties. *Arch. Biochem. Biophys.* 98:471–478.

81. Cunningham, L. W., Jr. 1954. Molecular-kinetic properties of crystalline diisopropyl phosphoryl trypsin. *J. Biol. Chem.* 211:13–19.

82. Cunningham, L. W., F. Tietze, …, H. Neurath. 1953. Molecular-kinetic properties of trypsin and related proteins. *Discuss. Faraday Soc.* 13:58–67.

83. Tietze, F. 1953. Molecular-kinetic properties of crystalline trypsinogen. *J. Biol. Chem.* 204:1–11.

84. Schwert, G. W., and S. Kaufman. 1951. The molecular size and shape of the pancreatic proteases. III. α-Chymotrypsin. *J. Biol. Chem.* 190:807–816.

85. Wilcox, P. E., J. Kraut, …, H. Neurath. 1957. The molecular weight of alpha-chymotrypsinogen. *Biochim. Biophys. Acta.* 24:72–78.

86. Schwert, G. W. 1951. The molecular size and shape of the pancreatic proteases. II. Chymotrypsinogen. *J. Biol. Chem.* 190:799–806.

87. Armstrong, J. M., D. V. Myers, …, J. T. Edsall. 1966. Purification and properties of human erythrocyte carbonic anhydrases. *J. Biol. Chem.* 241:5137–5149.

88. Edelhoch, H. 1957. The denaturation of pepsin. I. Macromolecular changes. *J. Am. Chem. Soc.* 79:6100–6109.

89. Nemoto, N., A. Koike, …, E. Doi. 1993. Dynamic light scattering of aqueous solutions of linear aggregates induced by thermal denaturation of ovalbumin. *Biopolymers.* 33:551–559.

90. Lamm, O., and A. Polson. 1936. The determination of diffusion constants of proteins by a refractometric method. *Biochem. J.* 30:528–541.

91. Pedersen, K. O. 1945. Ultracentrifugal Studies on Serum and Serum Fractions. Almquist & Wiksells, Uppsala, Sweden.

92. Oncley, J. L., G. Scatchard, and A. Brown. 1947. Physical-chemical characteristics of certain of the proteins of normal human plasma. *J. Phys. Chem.* 51:184–198.

93. Charlwood, P. A. 1952. Sedimentation and diffusion of human albumins. I. Normal human albumins at a low concentration. *Biochem. J.* 51:113–118.

94. Wood, E., D. Dalgleish, and W. Bannister. 1971. Bovine erythrocyte cupro-zinc protein. 2. Physicochemical properties and circular dichroism. *Eur. J. Biochem.* 18:187–193.

95. Ogston, A. G. 1949. The Gouy diffusiometer; further calibration. *Proc. R. Soc. Lond. A Math. Phys. Sci.* 196:272–285.

96. Creeth, J. 1958. Studies of free diffusion in liquids with the Rayleigh method. III. The analysis of known mixtures and some preliminary investigations with proteins. *J. Phys. Chem.* 62:66–74.

97. Le Bon, C., T. Nicolai, …, J. G. Hollander. 1999. Self-diffusion and cooperative diffusion of globular proteins in solution. *J. Phys. Chem. B.* 103:10294–10299.

98. Beretta, S., G. Chirico, and G. Baldini. 2000. Short-range interactions of globular proteins at high ionic strengths. *Macromolecules.* 33:8663–8670.

99. Cecil, R., and A. G. Ogston. 1949. The sedimentation constant, diffusion constant and molecular weight of lactoglobulin. *Biochem. J.* 44:33–35.

100. Kunitz, M., and J. H. Northrop. 1935. Crystalline chymo-trypsin and chymo-trypsinogen : I. Isolation, crystallization, and general

properties of a new proteolytic enzyme and its precursor. *J. Gen. Physiol.* 18:433–458.

101. Wilkins, D. K., S. B. Grimshaw, …, L. J. Smith. 1999. Hydrodynamic radii of native and denatured proteins measured by pulse field gradient NMR techniques. *Biochemistry.* 38:16424–16431.
102. Kabat, E. A., M. Heidelberger, and A. E. Bezer. 1947. A study of the purification and properties of ricin. *J. Biol. Chem.* 168:629–639.
103. Riddiford, C. L., and B. R. Jennings. 1967. Kerr effect study of the aqueous solutions of three globular proteins. *Biopolymers.* 5:757–771.
104. Wu, J. Y., and J. T. Yang. 1970. Physicochemical characterization of citrate synthase and its subunits. *J. Biol. Chem.* 245:212–218.
105. Wong, S. C., D. C. Hall, and J. Josse. 1970. Constitutive inorganic pyrophosphatase of Escherichia coli. 3. Molecular weight and physical properties of the enzyme and its subunits. *J. Biol. Chem.* 245:4335–4345.
106. Jaenicke, R., and W. B. Gratzer. 1969. Cooperative and non-cooperative conformational effects of the coenzyme on yeast glyceraldehyde-3-phosphate dehydrogenase. *Eur. J. Biochem.* 10:158–164.
107. Jaenicke, R., E. Gregori, and M. Laepple. 1979. Conformational effects of coenzyme binding to porcine lactic dehydrogenase. *Biophys. Struct. Mech.* 6:57–65.
108. Glikina, M. V., and P. A. Finogenov. 1950. [Investigation of muscular aldolase in various stages of isolation]. *Biokhimiia.* 15:457–464.
109. Kawahara, K. 1969. Evaluation of diffusion coefficients of proteins from sedimentation boundary curves. *Biochemistry.* 8:2551–2557.
110. Taylor, J. F., A. A. Green, and G. T. Cori. 1948. Crystalline aldolase. *J. Biol. Chem.* 173:591–604.
111. Christen, P., H. Göschke, …, A. Schmid. 1965. [On the aldolase in rabbit liver: molecular weight, dissociation into sub-units. On aldolases. 5]. *Helv. Chim. Acta.* 48:1050–1056.
112. Buzzell, J. G., and C. Tanford. 1956. The effect of charge and ionic strength on the viscosity of ribonuclease. *J. Phys. Chem.* 60:1204–1207.
113. Wetlaufer, D. B. 1961. Osmometry and general characterization of alpha-lactalbumin. *C. R. Trav. Lab. Carlsberg.* 32:125–138.
114. Dolgikh, D. A., R. I. Gilmanshin, …, O. B. Ptitsyn. 1981. α-Lactalbumin: compact state with fluctuating tertiary structure? *FEBS Lett.* 136:311–315.
115. Tanford, C. 1968. Protein denaturation. *Adv. Protein Chem.* 23:121–282.
116. Luzzati, V., J. Witz, and A. Nicolaieff. 1961. Détermination de la masse et des dimensions des protéines en solution par la diffusion centrale des rayons X mesurée à l'échelle absolue: Exemple du lysozyme. *J. Mol. Biol.* 3:367–378.
117. Monkos, K. 1997. Concentration and temperature dependence of viscosity in lysozyme aqueous solutions. *Biochim Biophys Acta.* 1339:304–310.
118. Kamiyama, T., M. Morita, and T. Kimura. 2004. Rheological study of lysozyme in dimethyl sulfoxide + water solution at 298.15 K. *J. Chem. Eng. Data.* 49:1350–1353.
119. Harris, J. I. 1956. Effect of urea on trypsin and alpha-chymotrypsin. *Nature.* 177:471–473.
120. Kay, C. M., L. B. Smillie, and F. A. Hilderman. 1961. The molecular weight of trypsinogen. *J. Biol. Chem.* 236:118–121.
121. Wong, K. P., and C. Tanford. 1973. Denaturation of bovine carbonic anhydrase B by guanidine hydrochloride. A process involving separable sequential conformational transitions. *J. Biol. Chem.* 248:8518–8523.
122. Blumenfeld, O. O., J. Léonis, and G. E. Perlmann. 1960. The effect of guanidine hydrochloride on crystalline pepsin. *J. Biol. Chem.* 235:379–382.
123. Monkos, K. 2000. Viscosity analysis of the temperature dependence of the solution conformation of ovalbumin. *Biophys. Chem.* 85:7–16.
124. Holt, J. C., and J. M. Creeth. 1972. Studies of the denaturation and partial renaturation of ovalbumin. *Biochem. J.* 129:665–676.
125. Wetzel, R., M. Becker, …, G. Lassmann. 1980. Temperature behaviour of human serum albumin. *Eur. J. Biochem.* 104:469–478.
126. Muzammil, S., Y. Kumar, and S. Tayyab. 1999. Molten globule-like state of human serum albumin at low pH. *Eur. J. Biochem.* 266:26–32.
127. Monkos, K. 2004. On the hydrodynamics and temperature dependence of the solution conformation of human serum albumin from viscometry approach. *Biochim. Biophys. Acta.* 1700:27–34.
128. Phelps, R. A., and J. R. Cann. 1956. On the modification of conalbumin by acid. II. Effect of pH and salt concentration on the sedimentation behavior, viscosity and osmotic pressure of conalbumin solutions. *Arch. Biochem. Biophys.* 61:51–71.
129. McKenzie, H. A., and W. H. Sawyer. 1967. Effect of pH on β-lactoglobulins. *Nature.* 214:1101–1104.
130. Bull, H. B., and B. T. Currie. 1946. Osmotic pressure of B-lactoglobulin solutions. *J. Am. Chem. Soc.* 68:742–745.
131. Fox, K., V. Holsinger, …, M. Pallansch. 1967. Separation of β-lactoglobulin from other milk serum proteins by trichloroacetic acid. *J. Dairy Sci.* 50:1363–1367.
132. Cohn, E. J., and A. M. Prentiss. 1927. Studies in the physical chemistry of the proteins : VI. The activity coefficients of the ions in certain oxyhemoglobin solutions. *J. Gen. Physiol.* 8:619–639.
133. Castellino, F. J., and R. Barker. 1968. Examination of the dissociation of multichain proteins in guanidine hydrochloride by membrane osmometry. *Biochemistry.* 7:2207–2217.
134. Tyn, M. T., and T. W. Gusek. 1990. Prediction of diffusion coefficients of proteins. *Biotechnol. Bioeng.* 35:327–338.
135. Stellwagen, E., and H. K. Schachman. 1962. The dissociation and reconstitution of aldolase. *Biochemistry.* 1:1056–1069.
136. Hass, L. F. 1964. Aldolase dissociation into subunits by reaction with succinic anhydride. *Biochemistry.* 3:535–541.
137. Qureshi, S. H., B. Moza, …, F. Ahmad. 2003. Conformational and thermodynamic characterization of the molten globule state occurring during unfolding of cytochromes-c by weak salt denaturants. *Biochemistry.* 42:1684–1695.
138. Edelhoch, H., and R. Steiner. 1963. Structural transitions of soybean trypsin inhibitor II. The denaturated state in urea. *J. Biol. Chem.* 238:931–938.
139. Koerdel, J., N. J. Skelton, …, W. J. Chazin. 1992. Backbone dynamics of calcium-loaded calbindin D9k studied by two-dimensional proton-detected nitrogen-15 NMR spectroscopy. *Biochemistry.* 31:4856–4866.
140. Akke, M., N. J. Skelton, …, W. J. Chazin. 1993. Effects of ion binding on the backbone dynamics of calbindin D9k determined by 15N NMR relaxation. *Biochemistry.* 32:9832–9844.
141. Malmendal, A., G. Carlström, …, M. Akke. 1998. Sequence and context dependence of EF-hand loop dynamics. An 15N relaxation study of a calcium-binding site mutant of calbindin D9k. *Biochemistry.* 37:2586–2595.
142. Schneider, D. M., M. J. Dellwo, and A. J. Wand. 1992. Fast internal main-chain dynamics of human ubiquitin. *Biochemistry.* 31:3645–3652.
143. Tjandra, N., S. E. Feller, …, A. d. Bax. 1995. Rotational diffusion anisotropy of human ubiquitin from 15N NMR relaxation. *J. Am. Chem. Soc.* 117:12562–12566.
144. Ghose, R., D. Fushman, and D. Cowburn. 2001. Determination of the rotational diffusion tensor of macromolecules in solution from nmr relaxation data with a combination of exact and approximate methods–application to the determination of interdomain orientation in multidomain proteins. *J. Magn. Reson.* 149:204–217.
145. Kelly, G. P., F. W. Muskett, and D. Whitford. 1997. Analysis of backbone dynamics in cytochrome b5 using 15N-NMR relaxation measurements. *Eur. J. Biochem.* 245:349–354.
146. Kay, L. E., D. A. Torchia, and A. Bax. 1989. Backbone dynamics of proteins as studied by 15N inverse detected heteronuclear NMR spectroscopy: application to staphylococcal nuclease. *Biochemistry.* 28:8972–8979.

147. Alexandrescu, A. T., W. Jahnke, …, M. J. Blommers. 1996. Accretion of structure in staphylococcal nuclease: an 15N NMR relaxation study. *J. Mol. Biol.* 260:570–587.

148. Cole, R., and J. P. Loria. 2002. Evidence for flexibility in the function of ribonuclease A. *Biochemistry.* 41:6072–6081.

149. Kovrigin, E. L., R. Cole, and J. P. Loria. 2003. Temperature dependence of the backbone dynamics of ribonuclease A in the ground state and bound to the inhibitor 5′-phosphothymidine (3′-5′)pyrophosphate adenosine 3′-phosphate. *Biochemistry.* 42:5279–5291.

150. Buck, M., J. Boyd, …, C. M. Dobson. 1995. Structural determinants of protein dynamics: analysis of 15N NMR relaxation measurements for main-chain and side-chain nuclei of hen egg white lysozyme. *Biochemistry.* 34:4041–4055.

151. Mine, S., S. Tate, …, T. Imoto. 1999. Analysis of the relationship between enzyme activity and its internal motion using nuclear magnetic resonance: 15N relaxation studies of wild-type and mutant lysozyme. *J. Mol. Biol.* 286:1547–1565.

152. Ermolina, I. V., I. N. Ivoylov, and V. D. Fedotov. 1997. Dielectric relaxation, molecular motion and interprotein interactions in myoglobin solution. *J. Biomol. Struct. Dyn.* 15:381–392.

153. South, G., and E. Grant. 1972. Dielectric dispersion and dipole moment of myoglobin in water. *P. R. Soc. A.* 328:371–387.

154. Clore, G. M., P. C. Driscoll, …, A. M. Gronenborn. 1990. Analysis of the backbone dynamics of interleukin-1 beta using two-dimensional inverse detected heteronuclear 15N-1H NMR spectroscopy. *Biochemistry.* 29:7387–7401.

155. Purvis, D. H., and B. C. Mabbutt. 1997. Solution dynamics and secondary structure of murine leukemia inhibitory factor: a four-helix cytokine with a rigid CD loop. *Biochemistry.* 36:10146–10154.

156. Yao, S., D. K. Smith, …, R. S. Norton. 2000. Backbone dynamics measurements on leukemia inhibitory factor, a rigid four-helical bundle cytokine. *Protein Sci.* 9:671–682.

157. Nicholson, L. K., T. Yamazaki, …, P. K. Jadhav. 1995. Flexibility and function in HIV-1 protease. *Nat. Struct. Biol.* 2:274–280.

158. Zheng, Z., J. Czaplicki, and O. Jardetzky. 1995. Backbone dynamics of trp repressor studied by 15N NMR relaxation. *Biochemistry.* 34:5212–5223.

159. Remerowski, M. L., H. A. Pepermans, …, F. J. Van De Ven. 1996. Backbone dynamics of the 269-residue protease Savinase determined from 15N-NMR relaxation measurements. *Eur. J. Biochem.* 235:629–640.

160. Schlecht, P., A. Mayer, …, H. Vogel. 1969. Dielectric properties of hemoglobin and myoglobin. I. Influence of solvent and particle size on the dielectric dispersion. *Biopolymers.* 7:963–974.

161. Peng, J. W., and G. Wagner. 1992. Mapping of the spectral densities of N-H bond motions in eglin c using heteronuclear relaxation experiments. *Biochemistry.* 31:8571–8586.

162. Wong, K.-B., A. R. Fersht, and S. M. Freund. 1997. NMR 15N relaxation and structural studies reveal slow conformational exchange in barstar C40/82A. *J. Mol. Biol.* 268:494–511.

163. Sahu, S. C., A. K. Bhuyan, …, J. B. Udgaonkar. 2000. Backbone dynamics of barstar: a (15)N NMR relaxation study. *Proteins.* 41:460–474.

164. Rawitch, A. B. 1972. The rotational diffusion of bovine -lactalbumin: a comparison with egg white lysozyme. *Arch. Biochem. Biophys.* 151:22–27.

165. Mets, U., M. Pooga, …, K. Gast. 1988. Rotational diffusion studies of native and molten globule states of bovine alpha-lactalbumin. *Stud. Biophys.* 126:87–97.

166. Cherry, R. J., A. Cogoli, …, G. Semenza. 1976. A spectroscopic technique for measuring slow rotational diffusion of macromolecules. 1: preparation and properties of a triplet probe. *Biochemistry.* 15:3653–3656.

167. Wahl, P., S. N. Timasheff, and J. Auchet. 1969. Polarized fluorescence decay curves for β-lactoglobulin A in various states of association. *Biochemistry.* 8:2945–2949.

168. Jarymowycz, V. A., and M. J. Stone. 2006. Fast time scale dynamics of protein backbones: NMR relaxation methods, applications, and functional consequences. *Chem. Rev.* 106:1624–1671.